JGR Atmospheres

RESEARCH ARTICLE
10.1029/2019JD032130

Key Points:
- Large-scale models of atmospheric dynamics can reproduce the shape of the global circuit diurnal variation but underestimate its amplitude
- It is important to take into account both convective activity and the area covered by electrified clouds (estimated from precipitation)
- Simulations better agree with measurements in Northern Hemisphere winters; South America and Southern Asia determine annual variation

Correspondence to:
N. V. Ilin,
ilyin@appl.sci-nnov.ru

Citation:
Ilin, N. V., Slyunyaev, N. N., & Mareev, E. A. (2020). Toward a realistic representation of global electric circuit generators in models of atmospheric dynamics. *Journal of Geophysical Research: Atmospheres*, *125*, e2019JD032130. https://doi.org/10.1029/2019JD032130

Received 26 NOV 2019
Accepted 2 MAR 2020
Accepted article online 5 MAR 2020

Author Contributions
Conceptualization: Nikolay V. Ilin, Nikolay N. Slyunyaev, Evgeny A. Mareev
Methodology: Nikolay V. Ilin, Nikolay N. Slyunyaev, Evgeny A. Mareev
Software: Nikolay V. Ilin
Writing - Original Draft: Nikolay V. Ilin, Nikolay N. Slyunyaev, Evgeny A. Mareev
Formal Analysis: Nikolay N. Slyunyaev
Supervision: Evgeny A. Mareev
Visualization: Nikolay N. Slyunyaev
Writing - review & editing: Nikolay N. Slyunyaev

Toward a Realistic Representation of Global Electric Circuit Generators in Models of Atmospheric Dynamics

Nikolay V. Ilin[1], Nikolay N. Slyunyaev[1], and Evgeny A. Mareev[1]

[1]Institute of Applied Physics, Russian Academy of Sciences, Nizhny Novgorod, Russia

Abstract The diurnal variation of the global electric circuit (GEC) is simulated using the Weather Research and Forecasting model by estimating contributions of grid columns to the ionospheric potential (IP). A parameterization based on cutting off the grid columns with shallow convection and estimating the area covered by GEC generators (electrified clouds) in each column from the amount of precipitation yields the IP variation of the same shape as the classical Carnegie curve with a correlation coefficient of 0.97, although with a smaller peak-to-peak amplitude (18% against 34% of the mean) and maxima and minima shifted by 1–2 hr. It is shown that omission in the IP parameterization of either convective activity or the area covered by electrified clouds (estimated using the calculated precipitation) would result in poor similarity between the modeled IP variation and the classical Carnegie curve. The results of simulation show the best agreement with the Carnegie data during Northern Hemisphere winters; the shape of the simulated diurnal variation of the IP substantially changes throughout the year owing to the decrease of South America's contribution and the increase of Southern Asia's contribution in summer. The discrepancies between the results of modeling and the results of observations are probably caused by the limited ability of large-scale models to differentiate between electrified and nonelectrified clouds. Further improvement of the parameterization of the IP in models of atmospheric dynamics requires using finer grids, which should allow computing microphysical characteristics of clouds and estimating source currents more accurately.

1. Introduction

Within the concept of the global electric circuit (GEC), the entire atmosphere is regarded as a distributed electric network, in which the current is maintained by charge separation in thunderstorms and electrified shower clouds (ESCs; e.g., Mareev, 2010; Rycroft et al., 2008; Tinsley, 2008; Williams, 2009). In the regions where such clouds occur the current flows upward, in fair-weather regions it flows downward, and the Earth's surface and lower ionosphere complete the network. Over the past few decades, this global approach has become dominant in the discussion of many problems related to atmospheric electricity (e.g., Williams & Mareev, 2014).

GEC parameters which are obtained in field measurements include the electric field and electric current density at the Earth's surface in fair-weather regions. Another important parameter is the ionospheric potential (IP), the potential of the ionosphere relative to the Earth's surface, which is nearly the same at remote locations (Markson et al., 1999); the IP can be determined experimentally by integrating vertical profiles of the electric field obtained in balloon and aircraft measurements (Markson, 2007). Measurements of GEC parameters (including the fair-weather electric field and IP) are motivated not only by the fundamental scientific interest in atmospheric electricity but also by the fact that the variation of these parameters on different time scales reflects the evolution of the state of the Earth system and space environment (e.g., Mareev & Volodin, 2014; Markson, 2007; Rycroft et al., 2000).

Given that systematic measurements of the fair-weather electric field have started more than 100 years ago, it is hardly surprising that GEC variability has been being widely studied and analyzed for the past few decades. Of all the time scales discussed in the literature in this regard (diurnal, monthly, annual, year-to-year, etc.), the diurnal scale is probably the most investigated and definitely one of the most important for understanding the dynamics of the GEC. Note that measurements of the electric field at the Earth's surface are influenced by many local factors, hence to analyze its diurnal variation, one usually takes the mean over a large number of days.

An important milestone in the investigation of the diurnal variation of GEC parameters is related to the electric field measurements on board the Carnegie ship in 1915–1929 (Ault & Mauchly, 1926; Torreson et al., 1946); a review of those measurements and their analysis from a modern viewpoint are given by Harrison (2013). The most important result obtained during the Carnegie campaigns is that the dependence of the mean electric field on (universal) time of day looks nearly the same at different locations (Mauchly, 1921, 1923); the corresponding plot is now usually referred to as the Carnegie curve. In the following years measurements performed by different researchers have produced further evidence that the mean diurnal variation of the GEC is quite satisfactorily described by the classical Carnegie curve, not only for the fair-weather electric field but also for other GEC parameters such as the IP (e.g., Harrison, 2003; Markson, 1986; Mühleisen, 1977). At the same time it should be noted that strictly speaking, this curve does not show an annual mean owing to the nonuniform seasonal sampling in the Carnegie data and substantial seasonal variability of the GEC (Burns et al., 2017).

The usual interpretation of the Carnegie curve is based on the observed similarity between the diurnal variation of the mean electric field at the Earth's surface in fair-weather conditions, which the Carnegie curve represents, and the diurnal variation of global thunderstorm activity (Whipple, 1929; Whipple & Scrase, 1936). This allows one to regard the shape of the Carnegie curve as the superposition of diurnal cycles of thunderstorm activity over different continents, each of which has a notable maximum around 15:00–17:00 local time (e.g., Bailey et al., 2007). This observation constitutes important evidence in favor of the concept of the GEC, according to which the distribution of fields and currents in the entire atmosphere is maintained primarily by thunderstorm generators. The data recently derived from satellite and aircraft cloud observations (Liu et al., 2010; Mach et al., 2011) and from global lightning locating systems (Hutchins et al., 2014; Mezuman et al., 2014) support this finding as well, also reproducing the shape of the classical Carnegie curve.

From the perspective of the mathematical model of the GEC, the distribution of fields and currents in the atmosphere is determined by (i) the distribution of conductivity and (ii) the distribution of the charge separation current density inside electrified clouds; the latter constitutes the source term in the equations describing the GEC (e.g., Kalinin et al., 2014) and is therefore also called "source current density." Now that these equations are linear, the main parameters of the GEC (including the fair-weather electric field or conduction current density at any point and the IP) are proportional to this source term and respond linearly to its perturbations; at the same time it can be argued that atmospheric conductivity changes do not significantly affect the diurnal variation of GEC parameters (see section 3.2 below). In other words, in theoretical investigations of the GEC one can assume that the diurnal variation of its parameters is determined by the variation of its sources and not by the variation of the conductivity; as a consequence, the diurnal variation of different GEC parameters (the IP, the fair-weather electric field at the Earth's surface, etc.) looks more or less the same, which justifies speaking about "the diurnal variation of the GEC."

Thus, modeling the diurnal variation of GEC parameters reduces to simulating the distribution of source currents at different hours of the day, which, in turn, requires modeling the dynamics of electrified clouds on the planetary scale. The latter problem cannot be solved without recourse to numerical models of the general atmospheric circulation. However, such models usually have relatively large grid cells (with horizontal dimensions of about 100 km) and, by inference, cannot resolve individual clouds. In addition, general atmospheric circulation models existing today do not take electrical processes into consideration, which further complicates the simulation of GEC variation, inasmuch as only electrified clouds serve as GEC generators. Therefore, such problems pose considerable difficulties and have not been discussed in the literature until recent years.

Mareev and Volodin (2014) have been the first to simulate the diurnal variation of the GEC in a general circulation model. Using the climate model INMCM (Institute of Numerical Mathematics Coupled Model), they developed a parameterization for the contribution to the IP of each grid cell occupied by deep convection, assuming that the conductivity grows exponentially with increasing height. The idea behind this approach was to identify electrified clouds (which cannot be explicitly distinguished from nonelectrified ones in climate models) with deep convective clouds. The developed parameterization takes into account the effective area covered by such clouds in each grid cell, estimated on the basis of calculated precipitation, and the altitudes of their lower and upper boundaries, calculated within the model. The resulting diurnal variation of the IP obtained by Mareev and Volodin (2014) with this parameterization turned out to be more or less similar to that of the classical Carnegie curve, but with a smaller peak-to-peak variation.

Lucas et al. (2015) and Kalb et al. (2016) employed the model CESM (Community Earth System Model) to discuss the related problem of parameterizing contributions to the GEC from electrified clouds on the basis of their dynamical and microphysical parameters calculated in climate models (note that such calculations are based on special schemes and parameterizations, since large-scale models are unable to resolve individual clouds and small-scale processes). The parameters considered by Kalb et al. (2016) include convective mass flux, ice water path, and convective precipitation in the mixed phase region (where both ice particles and supercooled liquid water droplets are present, which is required for noninductive charging), assumed to be bounded by the 0 °C and −50 °C isotherms. Of these three parameters convective mass flux was found to provide the best characterization of the current distribution estimated from the TRMM (Tropical Rainfall Measuring Mission) satellite data.

Jánský et al. (2017) simulated the diurnal variation of GEC parameters (the IP, total current, fair-weather electric field at the Earth's surface) both by directly inferring GEC parameters from the CESM data (utilizing the parameterization developed by Kalb et al., 2016) or TRMM data and by calculating them in GEC models with the sources parameterized on the basis of these data. It is interesting that the graphs of the diurnal variation based on the TRMM data showed much better agreement with the classical Carnegie curve than those based on modeling with the CESM: The latter have smaller peak-to-peak amplitudes and reach their maxima about 5 hr earlier than the classical Carnegie curve.

Recently, Slyunyaev et al. (2019) have employed the Weather Research and Forecasting model (WRF) running globally to simulate the diurnal variations of regional contributions to the GEC using a modernized version of the parameterization suggested by Mareev and Volodin (2014) for contributions from grid cells to the IP. Two very important aspects of this modernized parameterization are (i) estimating the effective area covered by electrified clouds from calculated precipitation and (ii) isolating the regions occupied by deep convection on the basis of calculated convective available potential energy (CAPE). The use of a weather forecasting model was motivated by the fact that, as opposed to climate models, such models are able to reproduce the state and dynamics of the Earth system in more detail (in particular, they are able to simulate the diurnal variation of the atmospheric parameters using the most complete available meteorological data for the initialization). Using this approach, Slyunyaev et al. (2019) obtained the variation of the total IP of the shape nearly identical to that of the classical Carnegie curve, albeit with a smaller peak-to-peak amplitude and slightly shifted maxima and minima.

To summarize, it appears that all past attempts to simulate the diurnal variation of the GEC using large-scale models of atmospheric dynamics resulted in the underestimation of its peak-to-peak amplitude. The main reason for this is probably the inability of large-scale models to faithfully distinguish electrified clouds from nonelectrified ones. At the same time semiempirical approaches to the parameterization of source currents based on using satellite data make it possible to obtain a more realistic value of the peak-to-peak amplitude (e.g., Jánský et al., 2017; Peterson et al., 2017); this suggests that parameterizations of source currents in climate models and weather forecasting models can be further improved in order to achieve a full understanding of the coupling between the GEC and atmospheric dynamics.

In this paper we investigate how different factors influence the diurnal variation of the GEC and whether parameterizations of source currents (or, which is equivalent, of contributions to the GEC) based on atmospheric dynamics can be further improved without recourse to smaller-scale modeling. For specific calculations we use the WRF and the IP parameterization of Slyunyaev et al. (2019); the model and peculiarities of modeling technique are described in section 2, while section 3 contains a detailed discussion of the IP parameterization. In section 4 we analyze and discuss the diurnal variation of the IP calculated using this parameterization and its various modifications so as to investigate the effect of various factors on the Carnegie curve and analyze the seasonal dynamics of contributions to this curve from different regions. Section 5 contains concluding remarks.

2. Modeling the Atmospheric Dynamics

The WRF (more precisely, Advanced Research version of WRF, or WRF-ARW) is a numerical model of atmospheric dynamics, designed for both weather prediction and research (https://www.mmm.ucar.edu/

weather-research-and-forecasting-model; see also Skamarock et al., 2008; Powers et al., 2017). For the purpose of simulating the atmospheric dynamics within this study, the WRF (version 3.9.1) has been run globally. Since the ARW solver for the WRF works in Cartesian coordinates, the entire atmosphere within this model is mapped into a rectangular parallelepiped, whose three dimensions correspond to latitude, longitude, and height above ground level. Periodic boundary conditions are set at the two boundaries corresponding to the prime meridian, and polar filtering is used to avoid computational problems in a neighborhood of each of the two poles (Skamarock et al., 2008).

We used a $1^\circ \times 1^\circ$ latitude-longitude grid with 51 altitude levels from the Earth's surface to the 10-mbar level and time steps of 150 s. We chose the following set of physics schemes for the WRF model: mp_physics = 2, ra_lw_physics = 4, ra_sw_physics = 4, radt = 30, sf_sfclay_physics = 1, sf_surface_physics = 2, bl_pbl_physics = 1, and cu_physics = 2. The most important options in this list are the widely used Purdue Lin microphysics scheme (Lin et al., 1983) and Betts-Miller-Janjić scheme of convection (Janjić, 1994, 2000); in our numerical experiments these schemes have proved most stable for global modeling. Given that we used a large-scale grid, precipitation was calculated on the basis of the parameterization of convection (so-called convective rain).

The NCEP (National Centers for Environmental Prediction) Global Data Assimilation System (GDAS)/FNL 0.25 data set (https://rda.ucar.edu/datasets/ds083.3) was used to initialize the WRF model. This data set contains the results of operational global analysis and forecast on a $0.25^\circ \times 0.25^\circ$ grid (FNL 0.25, where FNL stands for "final") prepared every 6 hr (at 0:00, 6:00, 12:00, and 18:00 UTC) with the GFS (Global Forecast System) model on the basis of the data collected by the GDAS.

The atmospheric dynamics simulated by the WRF is most reliable during a time period between about 12 and 48 hr from the model initiation. The first 12 hr are usually unrealistic, since the model needs some time to achieve the correct reproduction of the data absent in initial conditions (e.g., precipitation, clouds, and vertical wind speed). The results of modeling after 48 hr are less reliable owing to systematic errors in precipitation parameterizations used in weather forecasting models; a more accurate simulation is obtained by simply restarting the model for the next day with new initial conditions. For further discussion of these issues, see Appendix A.

For this study we have performed 732 48-hr free runs of the WRF starting at 0:00 UTC and 12:00 UTC on every day from 31 December 2015 to 30 December 2016; this has given us a complete picture of the state of the atmosphere for the year 2016. The choice of a 1-year period for the investigation of the GEC diurnal variation is motivated by the fact that 1 year is clearly sufficient for obtaining realistic mean values, whereas the variation of the global conductivity distribution (significantly affected by 11-year solar cycles) on this time scale can be neglected. Another reason to choose the year 2016 is that the NCEP GDAS/FNL 0.25 data set is available since the middle of 2015, while the data available for earlier periods are less accurate.

3. Parameterization of the Ionospheric Potential

In this section we describe the IP parameterization suggested by Slyunyaev et al. (2019) for the WRF model. This parameterization generally follows the ideas which underlie the parameterization by Mareev and Volodin (2014), although the practical implementation of these ideas in the case of the WRF is somewhat different in view of essential distinctions between climate models and weather forecasting models. Considering that we want to address the problem of how different factors entering into this parameterization affect the GEC, here we discuss it in greater detail, compared to the brief description given in Slyunyaev et al. (2019).

3.1. Calculation of the IP

From a mathematical viewpoint, the GEC is described by the distribution of the electric potential ϕ inside the model atmosphere, which is bounded by the Earth's surface Γ_1 and the outer boundary Γ_2. If GEC generators of magnetospheric and ionospheric origin are not taken into account, the steady state of the GEC is described by the following equations:

$$\operatorname{div}\left(\sigma \quad \operatorname{grad} \quad \phi\right) = \operatorname{div}\mathbf{j}^{\mathrm{s}} \tag{1}$$

$$\oint_{\Gamma_1} \sigma \quad \operatorname{grad} \quad \phi \cdot \mathbf{n}\, \mathrm{d}S = \oint_{\Gamma_1} \mathbf{j}^{\mathrm{s}} \cdot \mathbf{n}\, \mathrm{d}S \tag{2}$$

$$\phi|_{\Gamma_1} = 0, \qquad \phi|_{\Gamma_2} = V; \tag{3}$$

here σ is the conductivity, $\mathbf{j}^{\mathrm{s}}$ is the source current density (describing charge separation inside electrified clouds), $\mathbf{n}$ stands for the unit normal, and V is the unknown value of the IP. These equations uniquely determine the spatial distribution of the potential ϕ, including the value V of the IP, once the distributions of σ and $\mathbf{j}^{\mathrm{s}}$ are specified (e.g., Kalinin et al., 2014).

If the Earth's orography is not taken into account, Γ_1 is a sphere; letting Γ_2 be another sphere concentric with Γ_1, it is convenient to describe points in the model atmosphere by the altitude z above sea level (identified with the Earth's surface), the latitude in radians λ, and the longitude in radians ψ. It turns out that if the conductivity is a function of z alone, one can express the IP analytically in terms of σ and $\mathbf{j}^{\mathrm{s}}$ by integrating equations (1)–(3). Indeed, it follows from (1) and (2) by the divergence theorem that

$$\oint_{z=\mathrm{const}} \sigma \quad \mathrm{grad} \quad \phi \cdot \mathbf{n}\, \mathrm{d}S = \oint_{z=\mathrm{const}} \mathbf{j}^{\mathrm{s}} \cdot \mathbf{n}\, \mathrm{d}S \tag{4}$$

for any sphere $z = \mathrm{const}$, lying between Γ_1 and Γ_2. If the conductivity does not depend on λ and ψ, equation (4) can be rewritten as

$$\sigma(z) \int_0^{2\pi} \int_{-\pi/2}^{\pi/2} \frac{\partial \phi}{\partial z}(z, \lambda, \psi) \cos\lambda \, \mathrm{d}\lambda \, d\psi = \int_0^{2\pi} \int_{-\pi/2}^{\pi/2} j_z^{\mathrm{s}}(z, \lambda, \psi) \cos\lambda \, \mathrm{d}\lambda \, d\psi,$$

or

$$\frac{\mathrm{d}}{\mathrm{d}z} \int_0^{2\pi} \int_{-\pi/2}^{\pi/2} \phi(z, \lambda, \psi) \cos\lambda \, \mathrm{d}\lambda \, \mathrm{d}\psi = \frac{1}{\sigma(z)} \int_0^{2\pi} \int_{-\pi/2}^{\pi/2} j_z^{\mathrm{s}}(z, \lambda, \psi) \cos\lambda \, \mathrm{d}\lambda \, \mathrm{d}\psi. \tag{5}$$

By integrating (5) over z using (3), we arrive at the following equation (cf. equation 11 in Slyunyaev et al., 2014):

$$V = \int_0^{h_{\mathrm{atm}}} \frac{1}{4\pi\sigma(z)} \int_0^{2\pi} \int_{-\pi/2}^{\pi/2} j_z^{\mathrm{s}}(z, \lambda, \psi) \cos\lambda \, \mathrm{d}\lambda \, \mathrm{d}\psi \, \mathrm{d}z,$$

where h_{atm} is the distance between Γ_1 and Γ_2 (i.e., the height of the model atmosphere). In other words, the total IP can be represented as

$$V = \frac{1}{S_{\mathrm{E}}} \oint \int_0^{h_{\mathrm{atm}}} \frac{j_z^{\mathrm{s}}(z, \lambda, \psi)\, \mathrm{d}z}{\sigma(z)} \, \mathrm{d}S, \tag{6}$$

where the outer integral is taken over the Earth's surface, whose total area is S_{E}. To rewrite this equation for the WRF, we simply replace the surface integration with a summation over grid columns, consisting of grid cells with the same latitude and longitude; thus, (6) turns into

$$V = \frac{1}{S_{\mathrm{E}}} \sum_i S_i \int_0^{h_{\mathrm{atm}}} \frac{(j_i^{\mathrm{s}})_z(z)\, \mathrm{d}z}{\sigma(z)}, \tag{7}$$

where $\mathbf{j}_i^{\mathrm{s}}(z)$ is the source current density profile in the ith grid column and S_i is the area covered by this column.

3.2. Conductivity Distribution

Here we shall not take into account possible evolution of the conductivity distribution in time; there are several reasons for it. First, the observed pronounced correlation between the diurnal variation of the GEC and the diurnal cycle of global thunderstorm activity implies that the former is primarily determined by the variation of sources rather than by the variation of conductivity. Second, this hypothesis is further supported by the theory of the GEC: In view of the fact that equations (1)–(3) are linear, the IP (as well as other parameters of the GEC) is proportional to $\mathbf{j}^{\mathrm{s}}$ and responds linearly to its perturbations; at the same time elementary estimates show that the sensitivity of the IP to the perturbations of σ is usually lower (Slyunyaev et al., 2015). Third, significant global conductivity perturbations in the atmosphere (see, e.g., Rycroft et al., 2008) usually have either a very large time scale (e.g., in the case of 11-year solar cycles) or a rather small time scale (e.g., in the case of solar energetic particle events) and, by inference, have little effect on the diurnal variation of GEC parameters averaged over several months. Thus, the diurnal variation of the GEC is definitely determined by the diurnal cycle of its sources and not by the variation of the conductivity. Let us also note that conductivity changes on a diurnal time scale (e.g., due to diurnal cycles of radon and aerosols) are not likely to be global in their nature (at least their dynamics is not taken into account in large-scale conductivity parameterizations; see, e.g., Tinsley & Zhou, 2006), and there is no reason to expect that they would affect the resulting relative IP variation substantially.

We have already seen that the assumption of a uniform conductivity profile all over the Earth's surface considerably simplifies the problem, allowing one to express the IP analytically by means of equation (6) or (7). In case of using more elaborate conductivity parameterizations with σ also depending on λ and ψ, the IP can also be estimated in terms of σ and $\mathbf{j}^{\mathrm{s}}$, although the equations expressing such estimates are usually approximate and rather cumbersome. Once again dividing the atmosphere into large-scale grid columns, let us denote the conductivity and source current density in the ith such column as $\sigma_i(z)$ and $\mathbf{j}_i^{\mathrm{s}}(z)$, respectively; in this case, assuming that in each column the problem is nearly one dimensional, one can show that (see equation (23) in Slyunyaev et al., 2014)

$$V \approx \sum_i \left(S_i \int_0^{h_{\mathrm{atm}}} \frac{(j_i^{\mathrm{s}})_z(z)\,\mathrm{d}z}{\sigma_i(z)} \bigg/ \int_0^{h_{\mathrm{atm}}} \frac{\mathrm{d}z}{\sigma_i(z)} \right) \Bigg/ \sum_i \left(S_i \bigg/ \int_0^{h_{\mathrm{atm}}} \frac{\mathrm{d}z}{\sigma_i(z)} \right). \tag{8}$$

Actually (8) is nothing but a reformulation of Ohm's law for the entire GEC; note that it reduces to (7) if $\sigma_i(z) \equiv \sigma(z)$ for all i.

However, for the purpose of studying the diurnal variation of the IP it is sufficient to use equation (7) with a simple exponential conductivity profile

$$\sigma(z) = \sigma_0 \exp\left(\frac{z}{H}\right), \tag{9}$$

which adequately describes the main aspects of the real conductivity distribution. This assumption involves three major simplifications, each of which, however, turns out to be not critical for our study.

First, we ignore the effect of radon and aerosols on the conductivity. Although these two factors affect the integrals in (8) and their effect is nonuniform, being more pronounced over land than over oceans (e.g., Tinsley & Zhou, 2006), it is not hard to justify their neglect. To begin with, the denominator of (8), which actually constitutes the global resistance of the atmosphere, does not have any diurnal variation at all (since we have neglected the variation of conductivity with time), hence the relative IP variation (in which we are interested in this study) is completely determined by the numerator. In the numerator only the summands corresponding to source regions are nonzero, which allows us to rewrite it as

$$\begin{aligned}
&\sum_i \left(S_i \int_0^{h_{\mathrm{atm}}} \frac{(j_i^{\mathrm{s}})_z(z)\,\mathrm{d}z}{\sigma_i(z)} \bigg/ \int_0^{h_{\mathrm{atm}}} \frac{\mathrm{d}z}{\sigma_i(z)} \right) \\
&= \sum_{\substack{i:\,\text{source}\\ \text{columns}}} \left(S_i \int_0^{h_{\mathrm{atm}}} \frac{(j_i^{\mathrm{s}})_z(z)\,\mathrm{d}z}{\sigma_i(z)} \bigg/ \int_0^{h_{\mathrm{atm}}} \frac{\mathrm{d}z}{\sigma_i(z)} \right) \\
&= \sum_{\substack{i:\,\text{source}\\ \text{columns}}} \left(S_i \int_{\substack{\text{inside}\\ \text{the cloud}}} \frac{(j_i^{\mathrm{s}})_z(z)\,\mathrm{d}z}{\sigma_i(z)} \Bigg/ \left(\int_{\substack{\text{below}\\ \text{the cloud}}} \frac{\mathrm{d}z}{\sigma_i(z)} + \int_{\substack{\text{the}\\ \text{rest}}} \frac{\mathrm{d}z}{\sigma_i(z)} \right) \right).
\end{aligned}$$

Since the effects of radon and aerosols are most significant near the Earth's surface, the corresponding conductivity perturbations may affect only the integrals of $1/\sigma_i(z)$ taken over the regions below electrified clouds. However, considering that the effects of additional ionization due to radon (increasing conductivity) and ion attachment to aerosol particles (decreasing conductivity) partially compensate for each other, we can assume that such integrals do not change much when we take both of these factors into account. Moreover, strictly speaking, beneath electrified clouds we also need to consider additional ionization due to corona discharges (e.g., Standler & Winn, 1979), which is difficult to reliably estimate. Therefore, neglecting all these effects when considering the relative diurnal variation of the IP is probably the best option for the initial analysis of the problem.

Second, we neglect the effect of conductivity reduction owing to the attachment of ions to hydrometeors inside both electrified and nonelectrified clouds (e.g., Rust & Moore, 1974). Conductivity reduction inside nonelectrified clouds affects only the denominator of (8) and thus has no effect on the relative IP variation. As for electrified clouds, some studies indicate that conductivity reduction inside them may be counterbalanced by additional ionization owing to corona discharges from ice hydrometeors (Griffiths et al., 1974), and it is therefore unclear which amount of conductivity reduction is globally representative. Moreover, it is easy to see from equation (8) that if we introduce into (9) identical conductivity change by a factor of r inside all electrified clouds, this will not change the relative IP variation substantially. Indeed, in this case we will be able to transform the numerator of (8) as follows:

$$
\begin{aligned}
&\sum_i \left(S_i \int_0^{h_{\mathrm{atm}}} \frac{(j_i^{\mathrm{s}})_z(z)\,\mathrm{d}z}{\sigma_i(z)} \Bigg/ \int_0^{h_{\mathrm{atm}}} \frac{\mathrm{d}z}{\sigma_i(z)} \right) \\
&= \sum_{\substack{i:\,\text{source}\\ \text{columns}}} \left(S_i \int_0^{h_{\mathrm{atm}}} \frac{(j_i^{\mathrm{s}})_z(z)\,\mathrm{d}z}{\sigma_i(z)} \Bigg/ \int_0^{h_{\mathrm{atm}}} \frac{\mathrm{d}z}{\sigma_i(z)} \right) \\
&= \sum_{\substack{i:\,\text{source}\\ \text{columns}}} \left(S_i \int_{\substack{\text{inside}\\ \text{the cloud}}} \frac{(j_i^{\mathrm{s}})_z(z)\,\mathrm{d}z}{r\sigma(z)} \Bigg/ \left(\int_{\substack{\text{inside}\\ \text{the cloud}}} \frac{\mathrm{d}z}{r\sigma(z)} + \int_{\substack{\text{outside}\\ \text{the cloud}}} \frac{\mathrm{d}z}{\sigma(z)} \right) \right) \\
&= \sum_{\substack{i:\,\text{source}\\ \text{columns}}} \left(S_i \int_{\substack{\text{inside}\\ \text{the cloud}}} \frac{(j_i^{\mathrm{s}})_z(z)\,\mathrm{d}z}{\sigma(z)} \right) \Bigg/ \left(\int_{\substack{\text{inside}\\ \text{the cloud}}} \frac{\mathrm{d}z}{\sigma(z)} + r \int_{\substack{\text{outside}\\ \text{the cloud}}} \frac{\mathrm{d}z}{\sigma(z)} \right);
\end{aligned}
$$

this clearly has the same relative variation as the IP given by equation (7), provided that the geometry of different electrified clouds is more or less the same.

Finally, a uniform exponential profile (9) does not take into account the effect of enhanced conductivity at high latitudes. However, this enhancement does not substantially affect the variation of the IP. Indeed, in view of the fact that electrified clouds are mainly located at low latitudes, one can neglect high-latitude summands in the numerator of equation (8), while at low latitudes the conductivity profile does not change much and can be described by a single function (say, $\sigma(z)$); thus, the numerator of (8) may be transformed as

$$
\begin{aligned}
&\sum_i \left(S_i \int_0^{h_{\mathrm{atm}}} \frac{(j_i^{\mathrm{s}})_z(z)\,\mathrm{d}z}{\sigma_i(z)} \Bigg/ \int_0^{h_{\mathrm{atm}}} \frac{\mathrm{d}z}{\sigma_i(z)} \right) \\
&\approx \sum_{\substack{i:\,\text{low-lat}\\ \text{columns}}} \left(S_i \int_0^{h_{\mathrm{atm}}} \frac{(j_i^{\mathrm{s}})_z(z)\,\mathrm{d}z}{\sigma_i(z)} \Bigg/ \int_0^{h_{\mathrm{atm}}} \frac{\mathrm{d}z}{\sigma_i(z)} \right) \\
&\approx \sum_{\substack{i:\,\text{low-lat}\\ \text{columns}}} \left(S_i \int_0^{h_{\mathrm{atm}}} \frac{(j_i^{\mathrm{s}})_z(z)\,\mathrm{d}z}{\sigma(z)} \Bigg/ \int_0^{h_{\mathrm{atm}}} \frac{\mathrm{d}z}{\sigma(z)} \right) \\
&\approx \sum_i \left(S_i \int_0^{h_{\mathrm{atm}}} \frac{(j_i^{\mathrm{s}})_z(z)\,\mathrm{d}z}{\sigma(z)} \right) \Bigg/ \int_0^{h_{\mathrm{atm}}} \frac{\mathrm{d}z}{\sigma(z)},
\end{aligned}
$$

from which it follows that the diurnal variation of the IP predicted by (8) with enhanced high-latitude conductivity would be nearly identical (up to a constant coefficient) to that given by equation (7) with the uniform low-latitude conductivity profile extrapolated to the entire atmosphere.

For this study we shall use the uniform conductivity profile (9) with $\sigma_0 = 60$ fS/m and $H = 6$ km; this H is a characteristic scale height inferred from the analysis of more elaborate conductivity parameterizations of Tinsley and Zhou (2006) and Slyunyaev et al. (2015), and the choice of σ_0 actually has no effect on the relative variation of the IP, as one can readily see from equation (11) below.

3.3. Parameterization of Source Currents

Let us once again consider WRF grid columns, consisting of grid cells with the same latitude and longitude. We suppose that in the ith such column charge separation in electrified clouds occurs in the altitude range between z_i^{l} (the lower boundary) and z_i^{u} (the upper boundary), and the source current density inside this region of charge separation is directed upward and equal to J_i (whereas outside this region it is equal to zero). To make the representation of electrified clouds more faithful, we slightly generalize equation (7) by taking into account the fact that clouds cover only part of each WRF grid column. To this purpose we introduce a coefficient α_i representing the portion of the total area of the ith column covered by electrified clouds. Then, if the total area occupied by the column is S_i, the area covered by such clouds is $\alpha_i S_i$, and equation (6) yields

$$V = \frac{1}{S_\mathrm{E}} \sum_i \alpha_i S_i \int_0^{h_\mathrm{atm}} \frac{(j_i^\mathrm{s})_z(z)\,\mathrm{d}z}{\sigma(z)} \tag{10}$$

instead of (7).

Substituting the conductivity profile (9) for $\sigma(z)$ and the source current density profile

$$(j_i^\mathrm{s})_z(z) = \begin{cases} J_i, & z_i^\mathrm{l} \le z \le z_i^\mathrm{u}, \\ 0, & z < z_i^\mathrm{l} \mathrm{or} z > z_i^\mathrm{u} \end{cases}$$

for $(j_i^\mathrm{s})_z(z)$ in equation (10) and calculating the integral over z under these assumptions, we finally arrive at the following formula for the IP:

$$V = \sum_i \frac{J_i \alpha_i S_i H}{\sigma_0 S_\mathrm{E}} \left(\exp\left(-\frac{z_i^\mathrm{l}}{H}\right) - \exp\left(-\frac{z_i^\mathrm{u}}{H}\right) \right), \tag{11}$$

where the summation takes place over all grid columns.

Now we will discuss the parameterization of various quantities entering into equation (11) in more detail. In the following sections 3.4–3.6 we describe our basic parameterization of these quantities, while in section 4 other variants are also considered so as to elucidate which components of equation (11) matter most for the resulting diurnal variation of the IP.

3.4. Lower and Upper Boundaries of the Charge Separation Region

In the simplest approximation the region where charge separation occurs can be equated with the mixed phase region of the cloud, since noninductive charging, which is widely thought to be the dominant charge separation mechanism in most thunderstorms, requires the presence of both ice particles and supercooled liquid water droplets. Now that grid cells with a horizontal dimension of about 100 km do not allow resolving individual thunderstorms, we estimate the heights z_i^l and z_i^u for each grid column based on the temperature profile. It is known that the mixed phase region inside a cloud is bounded by the 0 °C and −38 °C isotherms (e.g., Pruppacher & Klett, 2010, Ch. 2.2); therefore we use the heights of these isotherms according to the model (more precisely, the heights of the nearest grid levels above them) as the values of z_i^l and z_i^u. In those regions where the temperature at the Earth's surface is already less than 0 °C (e.g., at high latitudes in winter or in high mountain areas) the lower boundary z_i^l occurs at the Earth's surface, but such regions do not give significant contribution to the IP owing to weak convective activity (see section 3.6 below).

Note that other studies may use different isotherms to approximate the upper boundary of the mixed phase region (e.g., Kalb et al., 2016 identified the upper boundary with the −50 °C isotherm) owing to the variation of the lowest temperature across different clouds. However, we will show below that the simulated diurnal variation of the IP is not very sensitive to the entire factor involving z_i^l and z_i^u (see section 4.3), hence it should not be very sensitive to the choice of the upper boundary either.

3.5. Area Covered by Clouds

By the introduction of the dimensionless parameter α_i, specifying the portion of the area of the grid column occupied by GEC generators, we try to take into consideration the fact that relatively large grid columns, generally speaking, are not completely covered by clouds. To parameterize α_i, we follow the approach suggested by Mareev and Volodin (2014), who assumed this coefficient to be proportional to the ratio P_i/W_i of the precipitation P_i per model time step (1 hr) and the total amount of precipitable water W_i (defined as the total mass of water vapor in the air column). In this study we also assume that

$$\alpha_i = k \cdot \frac{P_i}{W_i} \tag{12}$$

with some proportionality coefficient k, although we will not strictly specify the length of the time interval over which P_i is totaled and consider several different values. As further analysis will show, the resulting diurnal variation is actually not very sensitive to this length (see section 4.4).

To explain the physical motivation behind the parameterization given by (12), let us consider air parcels driven upward by convection. We assume that the amount of water that an air parcel precipitates during its entire ascent is proportional to the total amount W_i of precipitable water stored in the corresponding column (in particular, for a rough estimate we can assume that an air parcel eventually precipitates almost all the water that it contains, but given that actual precipitation efficiency may be smaller than 100%, we introduce a proportionality coefficient). This suggests that the ratio of the amount of water precipitated in the ith grid column during the corresponding time interval to the total amount of precipitable water stored in this column is proportional to the portion of the area within this column where convection occurs and, by inference, where clouds develop. Although time intervals that we shall use below for calculating precipitation are usually somewhat longer than typical air rise times, we can assume certain proportionality between amounts of precipitation totaled over different time intervals. In addition, as we have already noted, the analysis presented in section 4.4 below will prove that the simulated relative diurnal variation is indeed not very sensitive to the length of such time interval.

For our basic parameterization we assume that P_i is computed over a symmetric 2-hr period around the moment that W_i and other parameters are calculated (that is, a period starting 1 hr before that moment and ending 1 hr after it); the geographical distribution of the mean annual ratio P_i/W_i computed in this way is shown in Figure 1a. Other choices are also considered in Ssection 4.4, as well as a parameterization involving P_i without variable W_i.

3.6. Charge Separation Current Inside Thunderstorms

It follows from the discussion in the previous section that the coefficient α_i given by (12) characterizes the area covered by all clouds in each grid column; at the same time it is only electrified clouds that contribute to the GEC. Considering that α_i and the source current density J_i enter into equation (11) as the product $J_i \cdot \alpha_i$, we need to ensure that $J_i \equiv 0$ in grid columns without electrified clouds. When parameterizing J_i, we take into account the fact that electrified clouds are mostly characterized by deep convection. Estimation of contributions to the GEC based on convective activity is a common approach to modeling its diurnal variation. For example, in the parameterization of Mareev and Volodin (2014) the sum is taken over only those grid cells where, according to the INMCM, convection occurs; another example is the source current parameterization employed by Jánský et al. (2017), which is based on convective mass flux calculated within the CESM.

In this study we parameterize J_i using another quantity that characterizes convection, namely convective available potential energy (CAPE). We calculate CAPE with the function cape_2d of the wrf-python package (https://wrf-python.readthedocs.io/en/latest/user_api/generated/wrf.cape_2d.html), which estimates the maximum value of CAPE in each grid column by considering the air parcel with the highest equivalent potential temperature within the lowest 3 km above the ground level. For future reference, we denote the maximum value of CAPE in the ith grid column by ε_i; the geographical distribution of mean annual CAPE (ε_i) values is shown in Figure 1b.

Now we parameterize the charge separation current, setting the correspondence between ε_i and J_i by introducing the characteristic value j_0 and a function f:

$$J_i = j_0 f(\varepsilon_i) \tag{13}$$

We must choose the function f such that $f(\varepsilon)$ would approach zero as $\varepsilon \to 0$ and the value of $f(\varepsilon)$ at about 3 kJ/kg would be of order unity: If this is the case, the contributions from the regions with weak convective activity would be small, whereas the source current in intense convective systems (for which the assumed CAPE value of 3 kJ/kg is typical) would be of the order of j_0.

For our basic IP parameterization we choose f to be the following step function:

$$f(\varepsilon) = \begin{cases} 0, & \varepsilon < \varepsilon_0, \\ 1, & \varepsilon \geq \varepsilon_0, \end{cases} \tag{14}$$

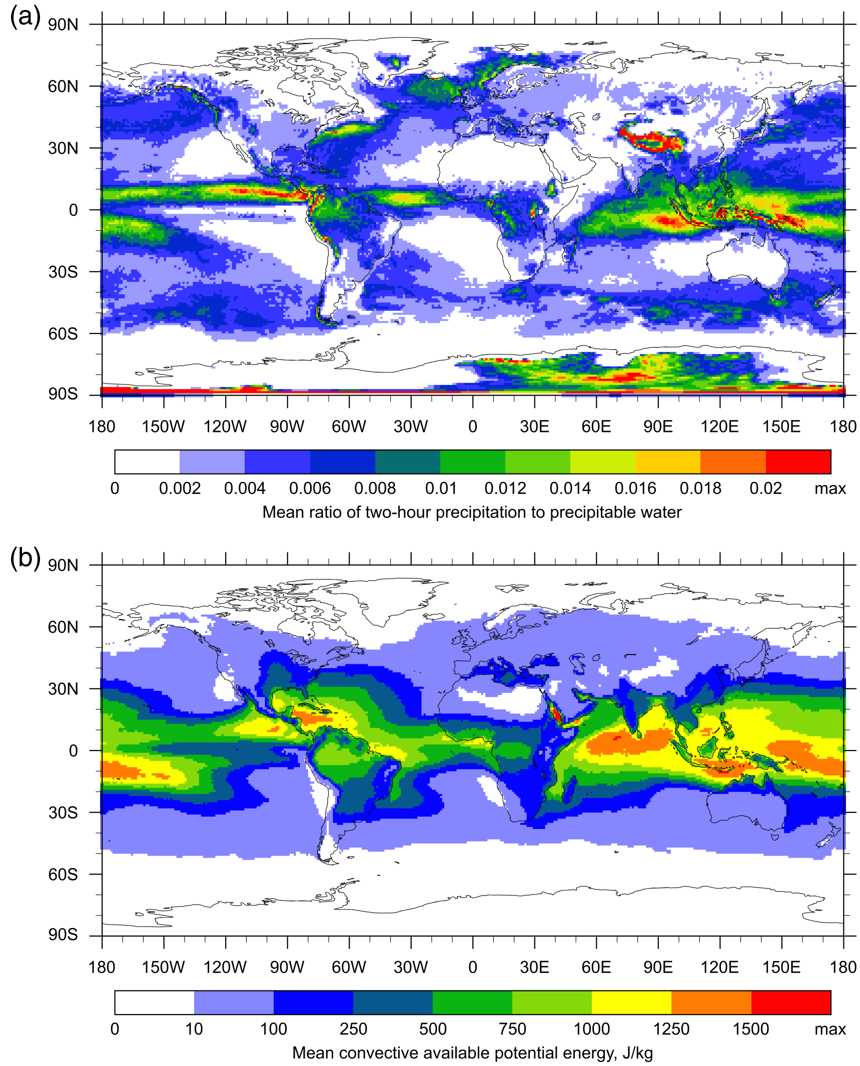

Figure 1. (a) Mean annual values of the ratio of precipitation (P_i) to the amount of precipitable water (W_i), where P_i is totaled over a symmetric 2-hr interval around the moment at which W_i is computed. (b) Mean annual values of maximum CAPE (ε_i). Adapted from Slyunyaev et al. (2019).

where ε_0 is the threshold CAPE value, which we take equal to 1 kJ/kg. In other words, we assume that the charging current in a grid column is zero unless model-predicted maximum CAPE is greater than 1 kJ/kg; the choice of this critical value is discussed in section 4.5. The idea of setting such a threshold is to single out the regions occupied by deep convection, which we have identified with the regions where electrified clouds occur. Note that CAPE values estimated in large-scale models of atmospheric dynamics do not directly correspond to those found in observations and are in fact some mean values calculated by using the same procedure. However, in our study we use CAPE only as a measure of convective activity, for which purpose such values are appropriate. Other natural choices of f are considered in section 4.5.

Once we have chosen f, it remains only to choose the parameter j_0. Unfortunately, there are little available data regarding charge separation currents inside thunderstorms and other electrified clouds. Aircraft observations (e.g., Mach et al., 2011) are usually directed toward measuring Wilson currents, which flow upward above clouds and may be substantially different from source currents inside them (Slyunyaev & Zhidkov, 2016). It is generally thought that source current densities are of the order of some nA m^{-2}, but specific values for model simulations are usually chosen by demanding that the values of global parameters (such as the IP) be realistic. Therefore, noting from equations (11) and (13) that the IP in our parameterization is proportional to the value of j_0, we can first perform necessary calculations with an arbitrary value of j_0 and then adjust it such that the mean IP would be equal to about 240 kV.

4. Results and Discussion

4.1. Basic Parameterization of the Ionospheric Potential: Annual-Average Diurnal Variation

For further discussion, it is convenient to rewrite equation (11), using (13), as

$$V = \sum_i \frac{j_0 S_i H}{\sigma_0 S_\mathrm{E}} \cdot f(\varepsilon_i) \cdot \alpha_i \cdot \left(\exp\left(-\frac{z_i^\mathrm{l}}{H}\right) - \exp\left(-\frac{z_i^\mathrm{u}}{H}\right)\right), \tag{15}$$

thus emphasizing its structure. The contribution of the ith grid column to the total IP is the product of (i) the constant factor $j_0 S_i H/\left(\sigma_0 S_\mathrm{E}\right)$, (ii) the factor $f(\varepsilon_i)$, representing the source current density and parameterized in terms of CAPE, (iii) the factor α_i, representing the area covered by electrified clouds and parameterized in terms of precipitation, and (iv) the factor $\exp\left(-z_i^\mathrm{l}/H\right) - \exp\left(-z_i^\mathrm{u}/H\right)$, representing variable heights of cloud boundaries. As the basic parameterizations of these factors, in Section 3 we have assumed approximating z_i^l and z_i^u by the heights of the 0 °C and −38 °C isotherms for the height factor, equation (12) with P_i computed over a symmetric two-hour period around the moment that W_i is calculated for the precipitation factor, and equation (14) with $\varepsilon_0 = 1$ kJ/kg for the CAPE factor.

Equation (15) allows us to calculate the IP at each time step in every model run. However, to obtain the mean diurnal variation of the IP on the basis of the 732 48-hour WRF simulations (see Section 2), we must employ certain averaging procedures, which are described in detail in Appendix A.

The IP variation obtained from equation (15) with the basic parameterizations of all factors is shown in Figure 2a (adapted from Slyunyaev et al., 2019). The IP is shown as a fraction of the mean; if we assume that $k \sim 1$ in (12) and require that the mean IP be equal to 240 kV, we need to choose $j_0 \sim 6.4$ nA m^{-2}, which looks rather realistic. Note, however, that the actual value of k depends on the length of the time period over which we calculate P_i, hence so does the characteristic value j_0.

Figure 2b, also taken from Slyunyaev et al. (2019), compares the simulated IP variation with the classical Carnegie curve. More precisely, we use the four-term harmonic fit obtained by Harrison (2013) for the data of Cruise VII of the Carnegie ship, published by Torreson et al. (1946). It is easy to see that our simulated curve and the classical Carnegie curve have very similar shapes (the sample correlation coefficient calculated on the basis of comparing hourly values is equal to 0.97). However, a direct comparison of the two plots shown in Figure 2b indicates that the positions of the corresponding maxima and minima differ by 1 or 2 hr and the peak-to-peak variation of the simulated Carnegie curve is about 46% smaller than that of the classical one (18% of the mean against 34% of the mean).

4.2. Basic Parameterization of the Ionospheric Potential: Seasonal Dynamics of Diurnal Variation

We have seen in Figure 2b that the simulated diurnal variation of the IP, averaged over the full year, is nearly of the same shape as the classical Carnegie curve, albeit with a smaller peak-to-peak amplitude. However, it is known that the GEC has a substantial seasonal variability, whereas the Carnegie data (on which the classical curve is based) are not uniformly distributed over the year (e.g., Burns et al., 2017). Therefore, it is instructive to make seasonal comparisons between our simulations and the Carnegie data as well. Figures 2c–2f show the simulated diurnal variations of the IP, averaged over different 3-monthly periods (November–January, February–April, May–July, and August–October, hereinafter abbreviated as NDJ, FMA, MJJ, and ASO, respectively); to this end we have combined the results of simulations corresponding to different months of the year 2016, as explained in section 2. These plots are compared with the four-term harmonic fits to the Carnegie data pertaining to different seasons by Harrison (2013) and Burns et al. (2017). Note that seasonal Carnegie fits by Harrison (2013) and seasonal Carnegie fits by Burns et al. (2017) are slightly different, inasmuch as the former are based on the data of Cruise VII of the Carnegie ship (Torreson et al., 1946), while the latter combine these data with the data of earlier Cruises IV, V, and VI (Ault & Mauchly, 1926).

Figures 2c–2f indicate that our parameterization of the IP is more or less able to reproduce the shape of the diurnal variation of the GEC, but is not generally correct in predicting its magnitude and the hours of maxima and minima (see Table 1 for a detailed comparison of peak-to-peak amplitudes, hours of maxima and minima, and correlation coefficients). The agreement of the IP simulation with the Carnegie data

10.1029/2019JD032130

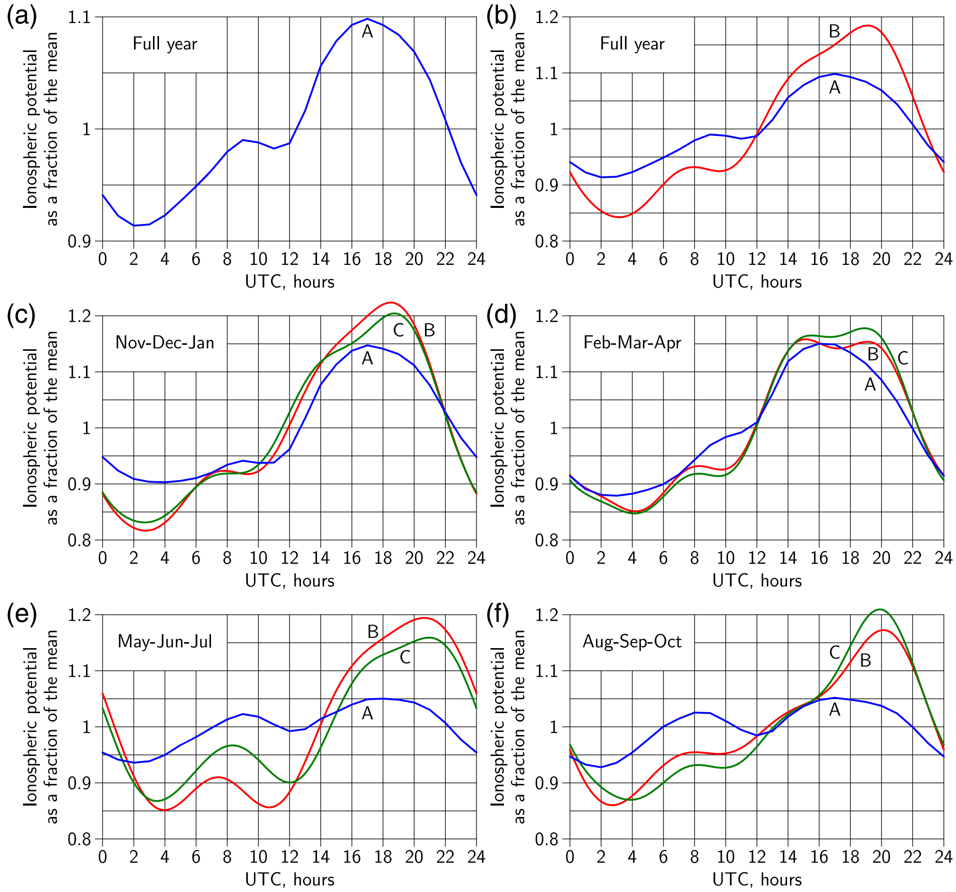

Figure 2. (a) Simulated diurnal variation of the IP with the basic parameterization of all factors (A, blue). Adapted from Slyunyaev et al. (2019). (b) Simulated IP variation (A, blue) and the classical Carnegie curve after Harrison (2013) (B, red). Adapted from Slyunyaev et al. (2019). (c)–(f) Comparison of the simulated diurnal variations of the IP corresponding to different seasons (A, blue) with the corresponding fits to the Carnegie data given by Harrison (2013) (B, red) and Burns et al. (2017) (C, green). In panels (a) and (b) the IP is presented as a fraction of the annual mean; in panels (c)–(f) the IP is shown as a fraction of the respective seasonal mean. Strictly speaking, the Carnegie data contain electric field values rather than the IP, but here we identify their relative variations.

is clearly better for (Northern Hemisphere) winter than for summer; in particular, the simulation more or less correctly estimates the peak-to-peak amplitude for FMA. On the other hand, this amplitude is notably underestimated in summer (MJJ and ASO), where the simulation predicts the secondary maximum to be of the same order as the primary one, which is not the case for seasonal curves based on observations (in particular, this results in a weaker correlation between simulations and observations for MJJ and ASO than for NDJ and FMA). Although electric field measurements in the Antarctic indicate that the difference between the two maxima is indeed smaller in summer months (Burns et al., 2017, Figure 1), the shapes of monthly averaged electric field variations obtained in those measurements are not always correctly reproduced by the monthly averaged IP variations inferred from our modeling (see Ilin et al., 2019, Figure 3). Also, note that our simulations generally yield earlier primary maxima and later secondary maxima than those found in the Carnegie data; the simulated minimum is mostly reached earlier than the observed one, except for NDJ. It is worth mentioning that the hours of maxima and minima of the GEC diurnal variation obtained in different studies do not always coincide; for example, seasonal splits of the diurnal variation of the total GEC current estimated on the basis of satellite and aircraft measurements by Blakeslee et al. (2014, Figure 14) are generally characterized by earlier primary maxima than those found in observations and thus better agree with our findings. However, the disagreement of amplitudes and seasonal dynamics is more conspicuous and apparently means that our parameterization of the IP (as well as other IP parameterizations based on convection) systematically overestimates or underestimates contributions of different regions to the total IP.

Table 1
Comparison of the Simulated GEC Diurnal Variation With That Based on the Carnegie Data (Figures 2b–2f) and Comparison of Contributions From Land and Ocean to the Simulated IP Variation (Figures 6a–6h)

	Full year	NDJ	FMA	MJJ	ASO
Peak-to-peak amplitude of the GEC diurnal variation (as a fraction of the mean)[a]					
(A): Results of simulation	18%	24%	27%	11%	12%
(B): Fit to Carnegie data (Harrison, 2013)	34%	41%	30%	34%	31%
(C): Fit to Carnegie data (Burns et al., 2017)		37%	33%	29%	34%
Hour of the primary maximum (UTC)[a]					
(A): Results of simulation	17	17	16	18	17
(B): Fit to Carnegie data (Harrison, 2013)	19.1	18.5	19.1	20.6	20.1
(C): Fit to Carnegie data (Burns et al., 2017)		18.7	18.9	20.9	19.9
Hour of the secondary maximum (UTC)[a]					
(A): Results of simulation	9	9	—	9	8
(B): Fit to Carnegie data (Harrison, 2013)	7.9	7.8	8.3	7.4	8.0
(C): Fit to Carnegie data (Burns et al., 2017)		8.2	8.3	8.3	8.2
Hour of the minimum (UTC)					
(A): Results of simulation	2	4	3	2	2
(B): Fit to Carnegie data (Harrison, 2013)	3.2	2.8	4.2	4.0	2.7
(C): Fit to Carnegie data (Burns et al., 2017)		2.7	4.2	3.5	3.9
Correlation coefficient (on the basis of hourly IP/electric field values)					
Correlation between (A) and (B)	0.97	0.98	0.98	0.57	0.74
Correlation between (A) and (C)		0.96	0.97	0.67	0.65
Contributions of land and ocean to the simulated diurnal variation of the GEC[b]					
Average contribution of land regions	46%	47%	43%	49%	47%
Average contribution of oceans	54%	53%	57%	51%	53%
Relative peak-to-peak amplitude for land	32%	45%	46%	18%	22%
Relative peak-to-peak amplitude for ocean	10%	9%	16%	10%	6%

[a]Additional maxima of the Fourier fits to the Carnegie data for FMA around 17:00 UTC, visible in Figure 2d, are neglected, since they have not been observed in later measurements. [b]For the partition of the Earth's surface into land and ocean assumed here, see the caption of Figure 6.

The discussion of seasonal dynamics of the diurnal variation of the GEC will continue in section 4.6. Now we shall discuss the role played by different factors appearing in formula (15).

4.3. The Role of the Height Factor

The basic parameterization of the height factor $\exp\left(-z_i^{\mathrm{l}}/H\right) - \exp\left(-z_i^{\mathrm{u}}/H\right)$, described in section 3.4, identifies the boundaries z_i^{l} and z_i^{u} of the charge separation region inside a cloud with the heights of the 0 °C and −38 °C isotherms, respectively. To analyze the role that this factor plays in the Carnegie curve, we assume that the values of z_i^{l} and z_i^{u} are the same all over the Earth, in which case the height factor also becomes constant. Comparing the resulting IP variation, shown in Figure 3a, with the basic curve, we see that the difference between the two plots is very small. Therefore we conclude that the height factor does not have a substantial effect on the diurnal variation of the GEC.

4.4. The Role of the Precipitation Factor

The basic parameterization of the precipitation factor α_i, defined as the portion of the area of the ith grid column occupied by electrified clouds, is expressed by equation (12) with P_i computed over the last hour and the next hour relative to the calculation of W_i and other parameters. The importance of this factor is clear from Figure 3b, showing the IP variation computed under the assumption $\alpha_i = 1$ (i.e., with a constant precipitation factor, which means that contributions from grid cells are primarily determined by the CAPE factor); comparing this new simulated variation with our basic curve, we observe that the magnitude of the new curve is much smaller and its main maximum is achieved several hours earlier.

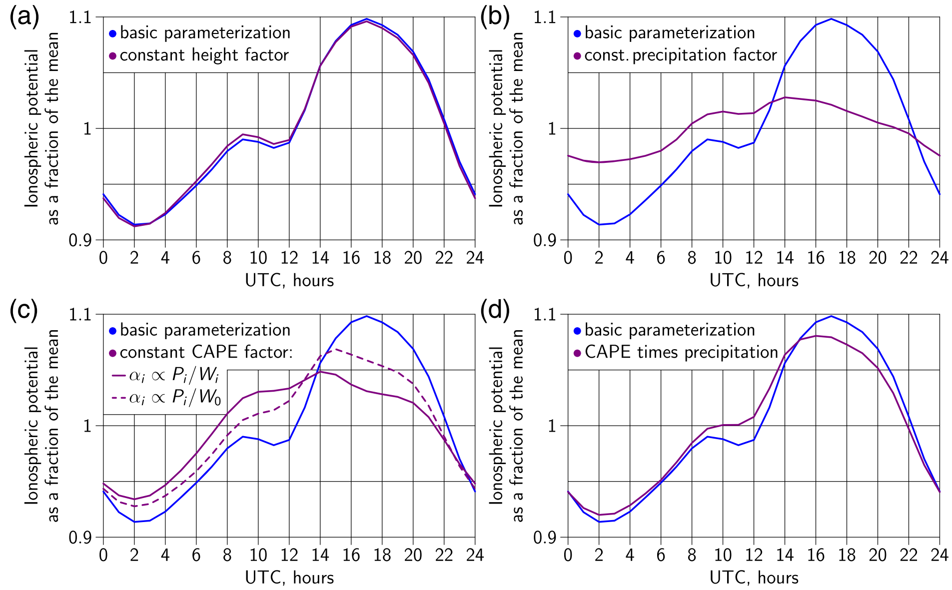

Figure 3. (a) Simulated IP variation with the basic parameterization (blue) and with a constant height factor (purple). (b) Simulated IP variation with the basic parameterization (blue) and with a constant precipitation factor (purple). (c) Simulated IP variation with the basic parameterization (blue) and with a constant CAPE factor (purple solid); also shown is the simulated IP variation with a constant CAPE factor and modified parameterization of the precipitation factor given by (16) (purple dashed). (d) Simulated IP variation with the basic parameterization (blue) and with the parameterization based on the product of CAPE and precipitation (purple).

Figure 4a shows the results of modifying the basic parameterization of α_i by calculating P_i over different time periods before and after the moment when W_i is computed. We see that the maxima and minima of the IP shift right when we calculate precipitation over longer time periods in the past and shift left when we calculate precipitation over longer time periods in the future. This is not surprising; for example, if we compute P_i over a time interval in the past and make this interval longer, the moment in time to which this P_i corresponds (estimated as the middle of the interval) shifts left, hence the whole graph of the IP shifts in the opposite direction. On the other hand, if we increase the length of the interval over which P_i is totaled without shifting it, the resulting IP variation does not change much. This can be seen in Figure 4b, showing the modification of the basic parameterization with P_i computed over the last 2 hr and the next 2 hr relative to the moment that W_i is obtained. Summarizing our observations, we conclude that the duration of the period over which precipitation P_i is totaled does not affect the IP variation very much, provided that the middle of this period remains the same; if it changes, the IP graph shifts left or right in the opposite direction.

Figure 4c shows the diurnal variation of the IP resulting from another modification of the basic parameterization of α_i. This time we replace the amount of precipitable water in the ith grid column W_i with a constant value W_0,

$$\alpha_i = k \cdot \frac{P_i}{W_0}, \tag{16}$$

thus neglecting the variation of W_i over the Earth's surface. Comparing the new curve with the basic one, we see that the variation of W_i has little effect on the IP variation. More detailed analysis shows that the average amount of precipitable water for large regions of the Earth's surface has a negligible diurnal variation. The amount of precipitable water stored in each particular grid column may have a more pronounced diurnal variation, but it is still much less in amplitude than that of the corresponding precipitation rate. Therefore, the dynamics of the area covered by electrified clouds is actually to a large extent determined by precipitation alone.

4.5. The Role of the CAPE Factor

The basic parameterization of the CAPE factor $f(\varepsilon_i)$, representing (up to a constant coefficient) the source current density, is expressed by equation (14) with $\varepsilon_0 = 1$ kJ/kg. The importance of this factor is supported by Figure 3c, showing the IP variation computed with $f = 1$ (i.e., with a constant CAPE factor, which means

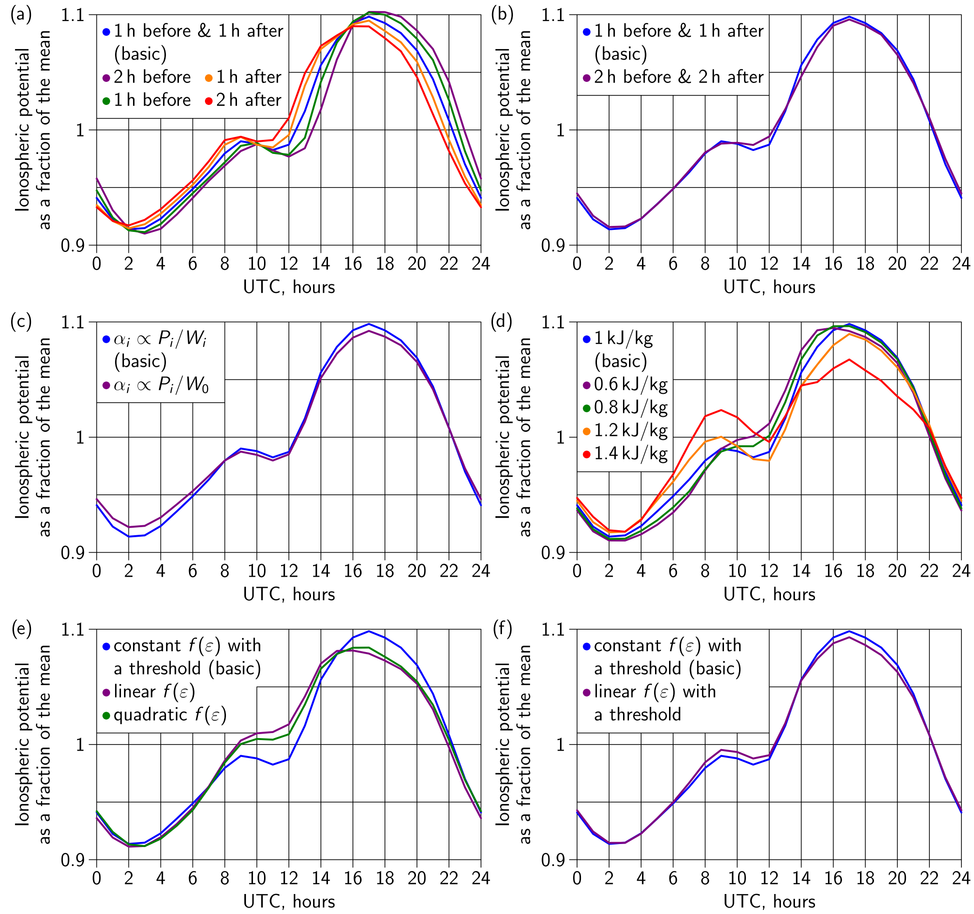

Figure 4. (a) Simulated IP variation with the basic parameterization (blue) and with the following modified parameterizations of the precipitation factor: equation (12) with P_i computed over the last 2 hr (purple), the last hour (green), the next hour (orange), and the next 2 hr (red) relative to the calculation of W_i. (b) Simulated IP variation with the basic parameterization (blue) and with the modified parameterization of the precipitation factor given by (12) with P_i computed over the last 2 hr and the next 2 hr relative to the calculation of W_i (purple). (c) Simulated IP variation with the basic parameterization (blue) and with the modified parameterization of the precipitation factor given by (16) (purple). (d) Simulated IP variation with the basic parameterization (blue) and with the following modified parameterizations of the CAPE factor: (14) with the threshold value ε_0 equal to 0.6 kJ/kg (purple), 0.8 kJ/kg (green), 1.2 kJ/kg (orange), and 1.4 kJ/kg (red). (e) Simulated IP variation with the basic parameterization (blue) and with the modified parameterizations of the CAPE factor given by (17) (purple) and (18) (green). (f) Simulated IP variation with the basic parameterization (blue) and with the modified parameterization of the CAPE factor given by (19) (purple).

that contributions from grid cells are primarily determined by the precipitation factor); comparing this new simulated variation with our basic curve, we observe that precipitation without CAPE cannot reproduce the IP variation correctly.

Note, however, that using the modified parameterization of the precipitation factor (16) instead of the basic equation (12) results in a better reproduction of the shape of the classical Carnegie curve even without the CAPE factor (compare solid purple and dashed purple lines in Figure 3c). This is apparently due to the fact that (16) better represents the contribution of regions where both P_i and W_i are very small and the ratio P_i/W_i cannot be reliably calculated within the model (e.g., the Antarctic and the Himalayas; see Figure 1a). There are actually no thunderstorm generators in such regions, and when we multiply the precipitation factor by the factor depending on CAPE they are effectively excluded; at the same time without the CAPE factor using (12) tends to overestimate the contribution of these regions, while (16) works relatively well. However, even (16) without the CAPE factor does not properly reproduce the shape of the diurnal variation of the IP, as Figure 3c shows.

Figure 4d shows the results of modifying the basic parameterization of f by using threshold CAPE values (ε_0) in (14) other than 1 kJ/kg. We observe that the values of ε_0 smaller than 1 kJ/kg yield similar IP variation curves, although the main maximum slightly shifts left with decreasing ε_0. On the other hand, if we further increase ε_0, the main maximum becomes smaller, while the second maximum becomes more pronounced. Comparing the curves presented in Figure 4d with the classical Carnegie curve (Figure 2b), we conclude that our choice of $\varepsilon_0 = 1$ kJ/kg for the basic parameterization of the CAPE factor indeed produces the most realistic IP variation.

Let us now consider other possible choices of the function f instead of (14). One natural idea is to assume a linear dependence between the charge separation current density and CAPE:

$$f(\varepsilon) = \frac{\varepsilon}{\varepsilon_{00}}, \tag{17}$$

where ε_{00} is the characteristic value of CAPE in intense convective systems. Another option is to use the quadratic formula

$$f(\varepsilon) = \left(\frac{\varepsilon}{\varepsilon_{00}}\right)^2; \tag{18}$$

the reasoning behind this assumption is that the charge separation current is proportional to both the relative velocity of colliding particles and the charge transferred in each collision, which, in its turn, is also related to the relative velocity by a power law with the exponent about 2 or 3 (at least in the case of noninductive charging; see Mareev & Dementyeva, 2017; Norville et al., 1991); thus, the charging current is proportional to the third or fourth power of the relative velocity, or to $\varepsilon_i^{3/2}$ or ε_i^2 (since CAPE is approximately proportional to the square of this velocity; see Williams & Stanfill, 2002). Figure 4e shows the diurnal variation of the IP computed with (17) and (18); it is clear that both these curves are similar in shape to our basic curve but reach their main maxima earlier. It is remarkable that (17) and (18), which are power laws with different exponents, produce nearly the same IP variation.

Finally, Figure 4f shows the IP variation corresponding to the parameterization that combines the aforementioned ideas of cutting off shallow convection and a linear dependence of the charge separation current on CAPE:

$$f(\varepsilon) = \begin{cases} 0, & \varepsilon < \varepsilon_0, \\ \varepsilon/\varepsilon_{00}, & \varepsilon \geq \varepsilon_0, \end{cases} \tag{19}$$

where $\varepsilon_0 = 1$ kJ/kg is assumed. We observe that the curves determined by (14) and (19) are very similar, notwithstanding that the former assumes identical contributions from the clouds with CAPE above the threshold and the latter assumes these contributions to be proportional to the CAPE value.

Summarizing the discussion above, we conclude that the position of the threshold has a greater effect on the simulated IP variation than the exact law relating the charging current and CAPE.

4.6. Further Discussion

We have seen that all natural modifications of our basic parameterization do not increase the magnitude of the simulated diurnal variation, which is required to reach quantitative agreement with the classical Carnegie curve. This is not a specific problem of the parameterization discussed in this paper; the IP variation simulated by Mareev and Volodin (2014) using the INMCM and the variation of GEC parameters simulated by Jánský et al. (2017) using the CESM also have smaller magnitudes than the classical Carnegie curve. Now we will discuss possible explanations of this discrepancy and suggest further ideas aimed at faithful modeling of the diurnal variation of the GEC.

It is usually thought that the shape of the Carnegie curve is primarily determined by continents, as thunderstorm activity over them has a noticeable diurnal variation, reaching its maximum around 16:00 local time; at the same time the contribution of oceans has a less pronounced variation (e.g., Mach et al., 2011, Figure 14), although, according to simulations, they also have their own diurnal cycle with a maximum between 2:00 and 6:00 local time (Slyunyaev et al., 2019, Figure 3). Figure 5 compares contributions of different land and ocean regions to the IP simulated using equation (15) with the basic parameterization (technically we just restrict the summation in (15) to the grid columns pertaining to each particular region). Here we use the same partition of the Earth's surface (see Figure 5a) that was previously used by Slyunyaev et al. (2019).

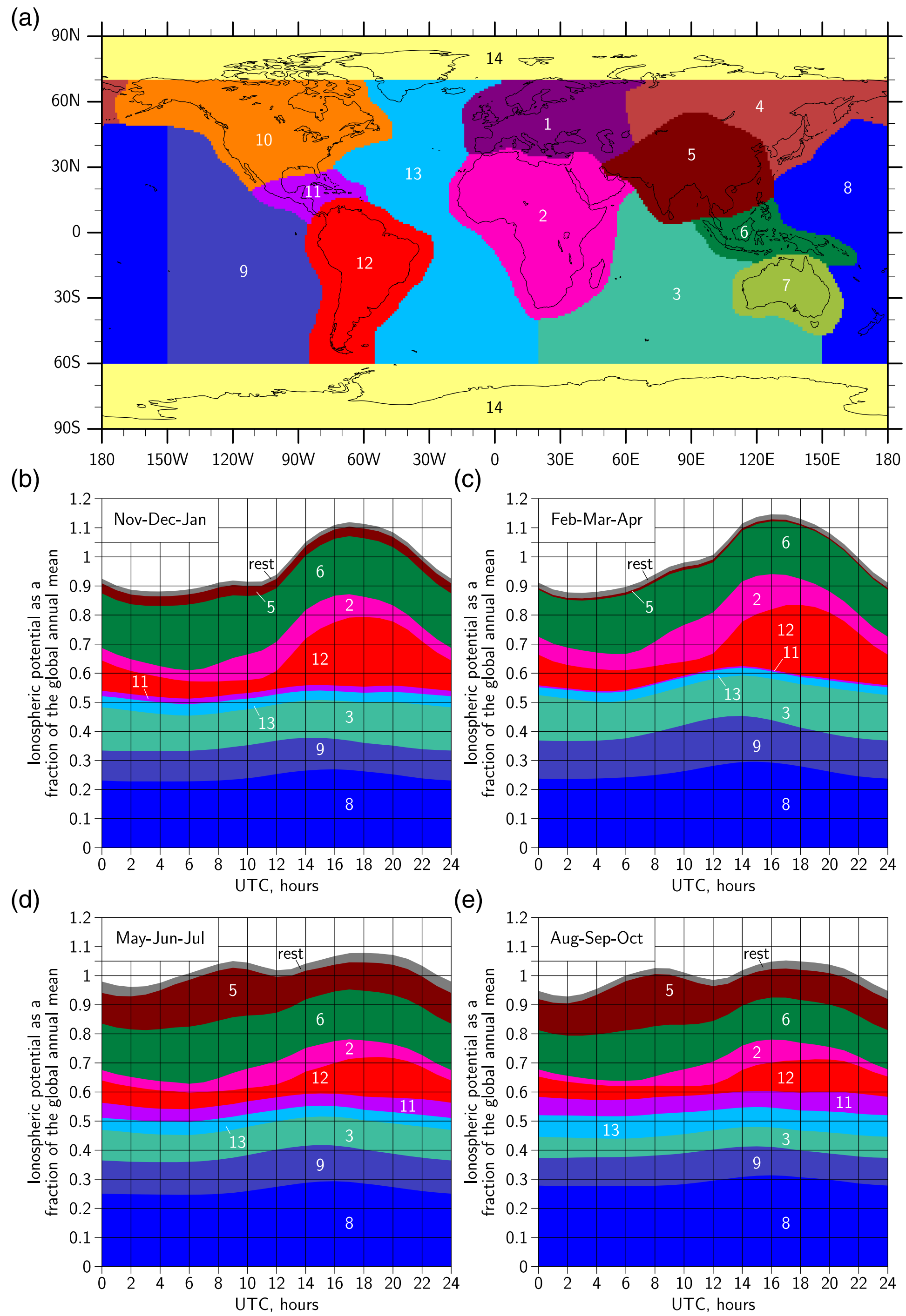

Figure 5. (a) Partition of the Earth's surface into regions for analyzing contributions to the IP, as in Slyunyaev et al. (2019). (b)–(e) Simulated diurnal variations of contributions of different regions to the IP in different seasons. The colors and labels in panels (b)–(e) are chosen according to panel (a), except for gray which represents the combined contribution of regions 1, 4, 7, and 10 (the contribution from region 14 is not included, being extremely small). All contributions to the IP are shown as fractions of the global annual mean.

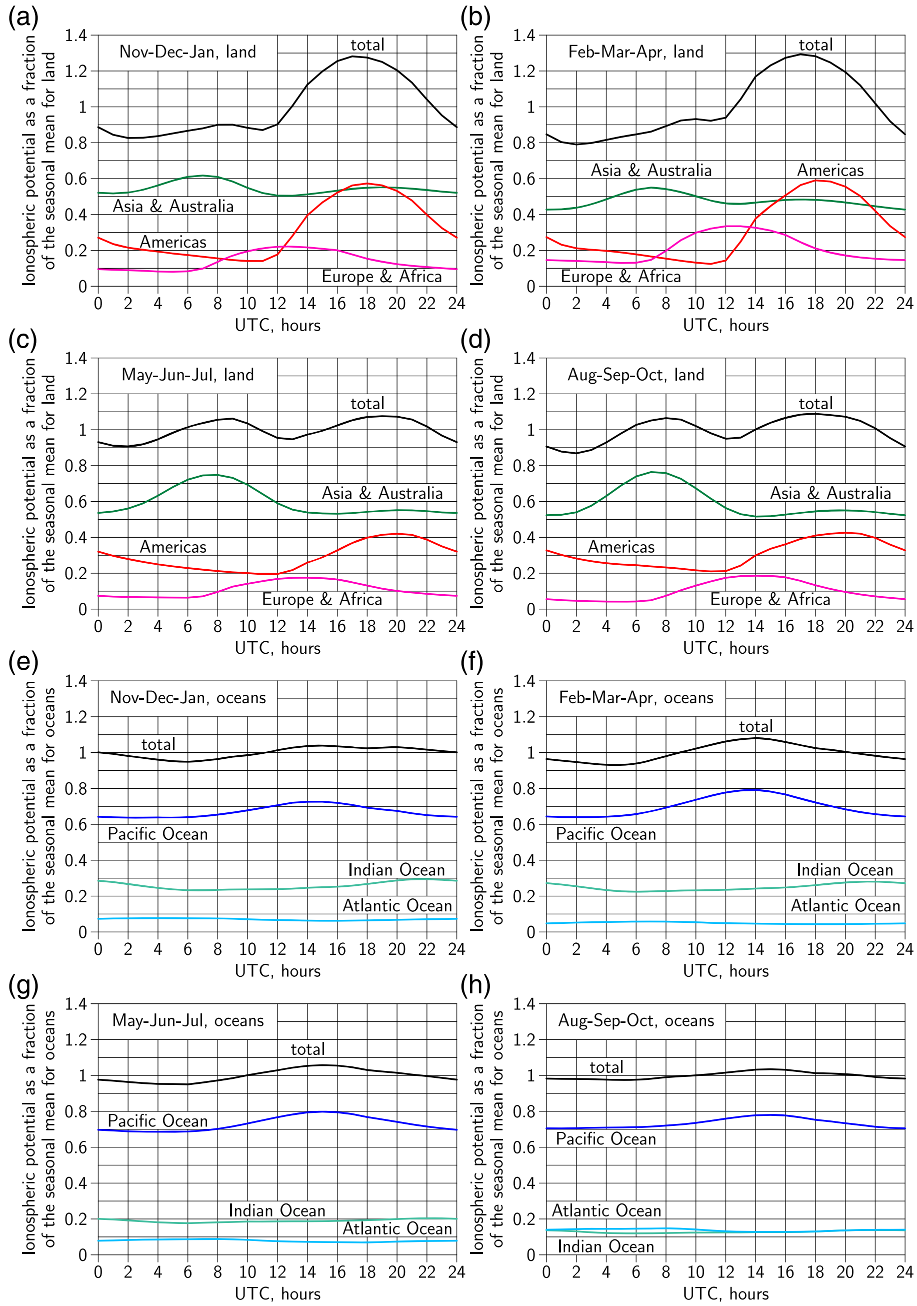

Figure 6. (a)–(d) Simulated diurnal variations of contributions of large land regions ("chimneys") to the IP in different seasons. (e)–(h) Simulated diurnal variations of contributions of oceans to the IP in different seasons. Here oceanic regions with many large islands are counted as land regions; the assumed partition of the Earth's surface corresponds to that shown in Figure 5a as follows: land regions include Europe and Africa (1, 2), Asia and Australia (4–7), and the Americas (10–12); oceanic regions include the Indian Ocean (3), the Pacific Ocean (8, 9), and the Atlantic Ocean (13). All contributions to the IP are shown as fractions of the respective seasonal means for the net contributions of land and oceans. Note that the colors do not directly correspond to those used in Figure 5.

We see that, according to the model, pure oceans and oceanic regions with many large islands (namely, the Maritime Continent and Middle America) make a much larger contribution to the GEC than continents, while the relative peak-to-peak variation of their total contribution is much smaller (see Figures 5b–5e).

To demonstrate the difference of amplitudes more clearly, in Figure 6 contributions to the IP from land regions and oceans are shown separately as fractions of their respective means. For convenience, we have grouped the regions shown in Figure 5a into larger areas, combining land regions (including the "intermediate" oceanic regions with many large islands) into the so-called "chimneys" of the GEC (Europe and Africa, Asia and Australia, and the Americas; see, e.g., Williams & Mareev, 2014) and combining oceanic regions into three major oceans (Indian, Pacific, and Atlantic); for the exact correspondence between these regions and those of Figure 5a, see the caption of Figure 6. Now it is easy to see that contributions of land regions (Figures 6a–6d) indeed have much greater diurnal peak-to-peak amplitudes than contributions of oceans (Figures 6e–6h). A quantitative comparison between seasonal means and diurnal peak-to-peak amplitudes of contributions to the IP from land and oceanic regions can be found in Table 1; for completeness, the values corresponding to the full year are also given there (although we do not plot the annually averaged counterparts of Figures 5b–5e and Figures 6a–6h).

Looking at Figures 5b–5e, which show how contributions from different regions make up the simulated IP variations for each season, we conclude that the simulated Carnegie curve is to a large extent determined by contributions from oceanic regions, South America, Africa, and Southern Asia. We see that the annual dynamics of the simulated diurnal variation (which we have seen in Figures 2c–2f) is primarily caused by two factors. First, the model-predicted contribution from South America, which is responsible for the main maximum of the Carnegie curve, is substantially reduced during MJJ and ASO. Second, the simulated contribution from Southern Asia, responsible for the secondary maximum of the IP, is substantially increased during the same two seasons.

Thin gray strips in the upper parts of Figures 5b–5e correspond to the combined contribution to the IP of Europe, Northern Asia, Northern America, and Australia; this contribution is dominated by Australia during NDJ and FMA and by Northern America during MJJ and ASO, but in either season it is too small to significantly affect the shape and magnitude of the global Carnegie curve. This may seem somewhat unexpected in the light of the fact that aircraft and satellite measurements imply a substantial contribution of North America to the global lightning flash rate (LFR), at least in (Northern Hemisphere) summer (see Mach et al., 2011, Figure 3; Blakeslee et al., 2014, Figure 6). It is unclear whether this is a consequence of modeling shortcomings or just a reflection of the fact that the IP is not proportional to LFR, being produced by both thunderstorms and ESCs.

The results of our simulations presented in Figures 5 and 6, and Table 1 agree with those of Mareev and Volodin (2014), whose model also produced a significant contribution of ocean convection to the IP with a nearly flat diurnal variation. At the same time estimates on the basis of aircraft and satellite measurements usually indicate that the contribution of oceans to the GEC is indeed flat but rather small (Blakeslee et al., 2014; Mach et al., 2011). Therefore, the underestimated peak-to-peak amplitude of the simulated IP variation (especially during MJJ and ASO) makes it natural to suppose that parameterizations based on evaluating contributions to the IP from convective activity tend to overestimate the role of oceans. Indeed, according to our simulations, land regions maintain an annual average of 46% of the total IP and oceans provide the remaining 54%, but their diurnal peak-to-peak amplitudes are 32% and 10% of the mean, respectively (see Table 1). When land and oceans are combined, this yields a peak-to-peak amplitude of 18%, which is about half as much as the amplitude of the classical Carnegie curve of 34%. Thus, if we reduced the contribution of oceans by about a factor of 2 or 3, we would obtain a considerably better IP variation, whose amplitude would be closer to that of the classical Carnegie curve.

However, even after this transformation the main maximum of the simulated IP variation would be reached about 2 hr earlier than that of the Carnegie curve. What is more important, this could not explain the conspicuous difference of amplitudes corresponding to winter (NDJ and FMA) and summer (MJJ and ASO), clearly visible in the results of simulations but absent in the Carnegie data (see Figures 2c–2f and Table 1) and in the data from other measurement campaigns (e.g., Burns et al., 2017; Figure 8). In addition, the whole idea of simply reducing the contribution of oceans lacks thorough substantiation on the basis of precise physical criteria; note that Mach et al. (2011) found that oceanic thunderstorms and ESCs actually produce greater mean currents than their land counterparts, although, strictly speaking, it would be more natural to compare current densities rather than total currents supplied by clouds.

A more consistent approach to improving the IP parameterization is based on adjusting the criteria used to single out electrified clouds. Liu et al. (2010), who analyzed the GEC diurnal variation on the basis of the

TRMM satellite data, divided all clouds without lightning into ESCs and nonelectrified clouds (of which the former contribute to the GEC and the latter do not do so) on the basis of estimating a 30-dBZ radar echo-top temperature. Although the criterion that they employed to distinguish ESCs from nonelectrified clouds was rather rough (apart from setting a lower limit for the cloud area, they arbitrarily associated ESCs with the temperature range characterized by the occurrence of lightning above 10%), a comparison of their mean annual geographical distribution of rainfall (Liu et al., 2010, Figure 3) with our Figure 1a suggests that a substantial fraction of grid columns characterized by a relatively large precipitation factor P_i/W_i is occupied by nonelectrified clouds. Of course, when we multiply the precipitation factor in equation (15) by the CAPE factor, we partially eliminate these clouds, as they are often characterized by shallow convection; notwithstanding, it seems that to achieve a more accurate IP parameterization, one should employ subtler criteria.

Recently, Peterson et al. (2015, 2017) have developed an algorithm for estimating the currents supplied by GEC generators on the basis of the data obtained with the TRMM and GPM (Global Precipitation Measurement) satellites. It has turned out, however, that the best agreement with the classical Carnegie curve is reached when only convective sources are taken into account, while all stratiform clouds are assumed to be nonelectrified (Peterson et al., 2017, Figure 2). This confirms our idea that to obtain a realistic Carnegie curve in simulation, one needs relatively subtle criteria that would allow accurate elimination of nonelectrified clouds. It should be emphasized that the algorithms used to differentiate between convective and stratiform clouds in satellite data are based upon analyzing the precipitation radar reflectivity profiles, something inaccessible in large-scale modeling. Also, note that aircraft measurements suggest that contributions from stratiform clouds to the Wilson current may be significant (Peterson et al., 2015), which makes the situation even more complicated; further research in this direction is probably needed to completely understand the implications of satellite results.

We have seen that both the precipitation factor and the CAPE factor in formula (15) are important for correct representation of the diurnal variation of the IP (see Figures 3b and 3c). It is interesting that a similar parameterization involving the product of CAPE and precipitation has been recently suggested to predict the geographical distribution and diurnal variation of LFR (Romps et al., 2014, 2018). As noted by Slyunyaev et al. (2019), from a physical perspective it seems more natural to identify this product with contributions to the GEC rather than with LFR, for it does not distinguish thunderstorms from ESCs. Figure 3d, showing the results of simulating the IP using equation (15) with linear $f(\varepsilon)$ and $\alpha_i \propto P_i/W_0$ (or, in other words, with the contributions of grid cells proportional to $\varepsilon_i \cdot P_i$), confirms this idea, considering that the resulting plot is more or less similar to the Carnegie curve obtained with our basic parameterization. It is not hard to see that these two parameterizations are actually based on the same ideas of reducing the impact of grid cells with low CAPE and estimating the area covered by convection on the basis of the amount of precipitation. In this regard, the product of CAPE and precipitation appears to characterize contributions to the GEC, and it is not unlikely that it provides a satisfactory proxy for LFR just because of the existing positive correlation between LFR and contributions to the IP.

To summarize, neither of the existing attempts to simulate the diurnal variation of the GEC using a climate or weather forecasting model has succeeded in obtaining a realistic peak-to-peak amplitude (cf. Mareev & Volodin, 2014, Figure 1a; Lucas et al., 2015, Figure 7; Jánský et al., 2017, Figure 3a). Our analysis has shown that when parameterizing the IP, it is important to take into account both convective activity (CAPE) and the area covered by electrified clouds (which can be inferred from the amount of precipitation), but neither of various reasonable alterations of our basic IP parameterization is able to significantly improve the agreement in magnitude between the simulated IP variation and the classical Carnegie curve. It appears that large-scale models with rather coarse grids do not allow complete elimination of nonelectrified clouds, and subtler criteria are needed. Such criteria may involve vertical profiles of microphysical characteristics of clouds calculated within weather forecasting models, such as radar reflectivity or mixing ratios and concentrations of hydrometeors of different types. One promising idea is to express source currents directly in terms of charged particle concentrations and vertical velocities; it is also possible that source currents depend on the regional aerosol content. However, accurate calculation of microphysical variables requires using finer grids, and the results presented in this article are probably the best that we can obtain from large-scale modeling.

5. Conclusions

1. The diurnal variation of the GEC can be simulated in climate and weather forecasting models by estimating contributions of grid columns to the IP. A parameterization based on cutting off the grid columns with weak convective activity and estimating the area covered by GEC generators (electrified clouds) in each column from the amount of precipitation, suggested by Slyunyaev et al. (2019), yields the IP variation whose shape is nearly identical to that of the classical Carnegie curve with a correlation coefficient of 0.97, albeit with a smaller peak-to-peak amplitude (18% against 34% of the mean) and maxima and minima shifted by 1–2 hr.
2. A more detailed analysis shows that it is crucially important to take into account in the IP parameterization both convective activity (cutting off shallow convection or at least reducing its contribution) and the area covered by electrified clouds (which can be estimated using the calculated precipitation). Omission of either of these factors results in poor similarity between the modeled IP variation and the classical Carnegie curve. At the same time the variability of the heights of cloud boundaries does not have a substantial effect on the diurnal variation of the IP.
3. When we parameterize the area covered by thunderstorms on the basis of precipitation, the duration of the time period over which precipitation is totaled does not affect the IP variation very much, provided that the middle of this period remains the same; if the middle of this period changes, the IP graph shifts in the opposite direction.
4. When we parameterize the charging current using CAPE, setting a threshold to cut off shallow convection yields better results than setting a power law (e.g., linear) dependence between the charging current and calculated CAPE. If such a threshold is set, its position has much greater effect on the IP variation than the exact law relating the charging current and CAPE above this threshold. The best results are obtained when the threshold is set at about 1 kJ/kg (for a $1^\circ \times 1^\circ$ grid).
5. The results of simulation show the best agreement with the results of measurements (e.g., the Carnegie data) during Northern Hemisphere winters. The shape of the simulated diurnal variation of the IP substantially changes throughout the year owing to the decrease of South America's contribution and the increase of Southern Asia's contribution in summer. It appears that the simulation generally overestimates the contribution of oceans (about one half of the mean IP, provided that the Maritime Continent and Middle America are counted as oceans), which are characterized by a smaller diurnal peak-to-peak amplitude than land regions (10% and 32% of their respective means).
6. The discrepancies between the results of modeling and the results of observations (including the apparent overestimation of the oceanic contribution to the GEC) are probably caused by the limited ability of large-scale models to differentiate between electrified and nonelectrified clouds. Further improvement of the parameterization of the IP in models of atmospheric dynamics is probably impossible without recourse to finer grids, which should allow computing microphysical characteristics of clouds and using them for a more accurate estimation of source currents.

Appendix A: Computation of the Mean Ionospheric Potential Variation

Here we discuss technical details of computing the mean diurnal variation of the IP using the WRF model and the parameterization of section 3 (or any its modification).

In every one of the 732 48-hr model runs (see section 2) we calculate the IP every hour by means of equation (15). As we have already noted in section 2, the results over the first 12 hr since the model initiation, when the data absent in initial conditions are not yet reproduced correctly, are not reliable. This is easy to see in Figure A1, which shows the evolution of the IP calculated by means of equation (15) with the parameterization of section 3, averaged over the 366 model runs initiated at 0:00 UTC and 366 model runs initiated at 12:00 UTC; for convenience, the contributions of land and ocean (according to the standard land/sea mask of the WRF model) to the total IP are shown in separate panels, considering that their variations have essentially different magnitudes.

It is clear that the plots corresponding to model runs starting at 0:00 UTC and 12:00 UTC have similar intervals of increase and decrease and local maxima and minima at nearly the same hours (after the natural 12-hr shift). However, neither of the plots exactly repeats itself after 24 hr, which is not surprising in view of the remark made in section 2 that precipitation parameterizations used in weather forecasting models are not perfect and probably contain systematic errors. This is one reason that we do not simulate the atmospheric

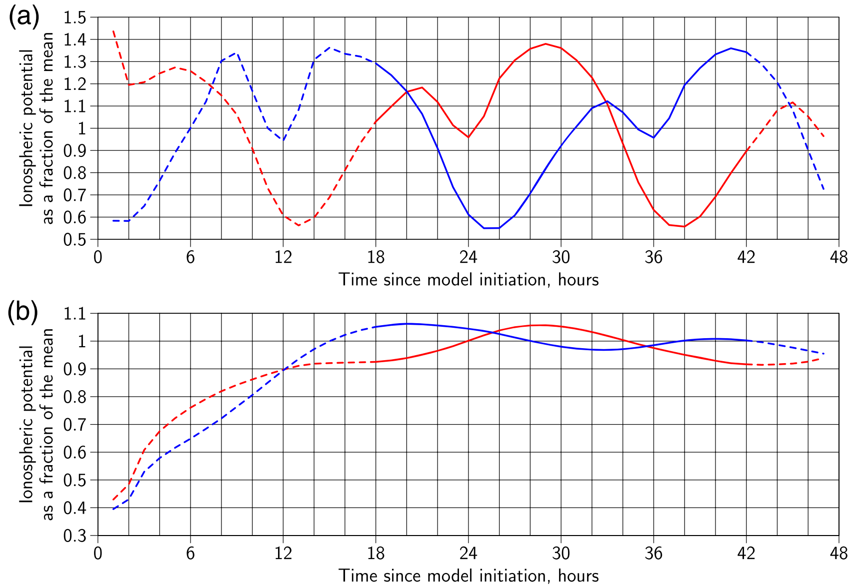

Figure A1. The evolution of land (a) and ocean (b) contributions to the IP calculated by means of equation (15) with the basic parameterization of section 3 in 48-hr WRF simulations, averaged over the 366 model runs initiated at 0:00 UTC (blue) and 366 model runs initiated at 12:00 UTC (red). In each panel the IP is shown as a fraction of the mean value over the time interval between 18 and 42 hr since model initiation; the dashed segments of the plots lie outside this time interval.

dynamics over time intervals longer than 48 hr but rather start separate model runs for each day of the year. Another reason behind this approach is the necessity to take into account the variability of the state of the ocean (e.g., the dynamics of the sea surface temperature) when modeling atmospheric dynamics on a time scale of several days; this variability is not explicitly taken into account by the WRF (but can be incorporated in the WRF from other sources). Finally, we would like to note that the equations that govern atmospheric dynamics generally have unstable solutions (that is, slight perturbations of initial conditions eventually result in a substantial modification of the calculated weather and climate variables). Therefore, simulation of atmospheric dynamics on large time scales requires additional adjustment procedures, which are common in general circulation models, but not in weather forecasting models, to which the WRF belongs. However, this instability becomes an important issue only when the simulated period includes several weeks.

Once again looking at Figure A1, we observe that in each case it takes even more than 12 hr for the IP variation to become quasiperiodic. In view of this observation, we restrict our attention to the time interval between 18 and 42 hr since the model initiation. To obtain a periodic curve representing the diurnal variation, we use the following "regularization" procedure. We consider two 24-hr data sets representing the IP evolution between 18 and 42 hr since the model initiation, (i) the average of the 366 model runs initiated at 0:00 UTC and (ii) the average of the 366 model runs initiated at 12:00 UTC. Obviously, the two data sets correspond to the 24-hr intervals starting and ending at 18:00 UTC and 6:00 UTC, respectively.

First, we make each of these data sets periodic by linearly adjusting IP values while keeping the mean value of the IP the same. More precisely, we add such linear function of time to the function representing the computed IP variation that the adjusted IP at 18 hr is equal to the adjusted IP at 42 hr, while the mean value of the adjusted IP over the interval between 18 and 42 hr is equal to that of the original (unadjusted) IP. The latter condition clearly amounts to demanding that the linear function be equal to zero at 30 hr (in the middle of the interval).

After the adjustment we have two 24-hr periodic data sets representing the IP evolution, one of them starting and ending at 18:00 UTC and the other starting and ending at 6:00 UTC. After appropriate shifting both these data sets represent the diurnal variation of the IP, and we take the average of these two variations as the final result. The main advantage of this approach, based on averaging the two model runs initiated with a 12-hr difference, is that it allows us to make the estimation of the diurnal variation more symmetrical and partially compensate for the variable accuracy of the model at different stages of a 48-hr simulation.

Acknowledgments
The authors are grateful to Gary Burns for providing the Fourier fits to the Carnegie data used in Burns et al. (2017). This work was supported by the Russian Science Foundation (Project 18-77-10061). The WRF-ARW model is available at this site (http://www2.mmm.ucar.edu/wrf/users/downloads.html); the NCEP GDAS/FNL 0.25 data set is available at this site (https://rda.ucar.edu/datasets/ds083.3). The complete description of simulation options is given in section 2. The developed IP parameterization and its modifications used in this study are completely described in sections 3 and 4 (the Python scripts and results are available at https://bitbucket.org/nilyin/jgr2019). The procedures used to compute the mean IP are completely described in Appendix A.

References

Ault, J. P., & Mauchly, S. J. (1926). Atmospheric electric results obtained aboard the Carnegie, 1915–1921, *Ocean magnetic and electric observations, 1915–1921*. Washington, D.C.: Carnegie Institution of Washington. Retrieved from https://archive.org/details/oceanmagneticele00carn (Carnegie Institution of Washington Publication 175).

Bailey, J. C., Blakeslee, R. J., Buechler, D. E., & Christian, H. J. (2007). Diurnal lightning distributions as observed by the Optical Transient Detector (OTD) and the Lightning Imaging Sensor (LIS). *Paper presented at the 13th Int. Conf. on Atmospheric Electricity*, Beijing.

Blakeslee, R. J., Mach, D. M., Bateman, M. G., & Bailey, J. C. (2014). Seasonal variations in the lightning diurnal cycle and implications for the global electric circuit. *Atmospheric Research*, *135–136*, 228–243. https://doi.org/10.1016/j.atmosres.2012.09.023

Burns, G. B., Frank-Kamenetsky, A. V., Tinsley, B. A., French, W. J., Grigioni, P., Camporeale, G., & Bering, E. A. (2017). Atmospheric global circuit variations from Vostok and Concordia electric field measurements. *Journal of the Atmospheric Sciences*, *74*(3), 783–800. https://doi.org/10.1175/JAS-D-16-0159.1

Griffiths, R. F., Latham, J., & Myers, V. (1974). The ionic conductivity of electrified clouds. *Quarterly Journal of the Royal Meteorological Society*, *100*(424), 181–190. https://doi.org/10.1002/qj.49710042405

Harrison, R. G. (2003). Twentieth-century atmospheric electrical measurements at the observatories of Kew, Eskdalemuir and Lerwick. *Weather*, *58*(1), 11–19. https://doi.org/10.1256/wea.239.01

Harrison, R. G. (2013). The Carnegie curve. *Surveys in Geophysics*, *34*(2), 209–232. https://doi.org/10.1007/s10712-012-9210-2

Hutchins, M. L., Holzworth, R. H., & Brundell, J. B. (2014). Diurnal variation of the global electric circuit from clustered thunderstorms. *Journal of Geophysical Research: Space Physics*, *119*, 620–629. https://doi.org/10.1002/2013JA019593

Ilin, N. V., Shatalina, M. V., & Slyunyaev, N. N. (2019). Modeling the seasonal dynamics of the diurnal variation of the global electric circuit. *Izvestiya, Atmospheric and Oceanic Physics*, *55*(5), 446–452. https://doi.org/10.1134/S0001433819050086

Janjić, Z. I. (1994). The step-mountain eta coordinate model: Further developments of the convection, viscous sublayer, and turbulence closure schemes. *Monthly Weather Review*, *122*(5), 927–945. https://doi.org/10.1175/1520-0493(1994)122<0927:TSMECM>2.0.CO;2

Janjić, Z. I. (2000). Comments on "Development and evaluation of a convection scheme for use in climate models". *Journal of the Atmospheric Sciences*, *57*(21), 3686–3686. https://doi.org/10.1175/1520-0469(2000)057<3686:CODAEO>2.0.CO;2

Jánský, J., Lucas, G. M., Kalb, C., Bayona, V., Peterson, M. J., Deierling, W., et al. (2017). Analysis of the diurnal variation of the global electric circuit obtained from different numerical models. *Journal of Geophysical Research: Atmospheres*, *122*, 12,906–12,917. https://doi.org/10.1002/2017JD026515

Kalb, C., Deierling, W., Baumgaertner, A., Peterson, M., Liu, C., & Mach, D. (2016). Parameterizing total storm conduction currents in the Community Earth System Model. *Journal of Geophysical Research: Atmospheres*, *121*, 13,715–13,734. https://doi.org/10.1002/2016JD025376

Kalinin, A. V., Slyunyaev, N. N., Mareev, E. A., & Zhidkov, A. A. (2014). Stationary and nonstationary models of the global electric circuit: Well-posedness, analytical relations, and numerical implementation. *Izvestiya, Atmospheric and Oceanic Physics*, *50*(3), 314–322. https://doi.org/10.1134/S0001433814030074

Lin, Y., Farley, R. D., & Orville, H. D. (1983). Bulk parameterization of the snow field in a cloud model. *Journal of Climate and Applied Meteorology*, *22*(6), 1065–1092. https://doi.org/10.1175/1520-0450(1983)022<1065:BPOTSF>2.0.CO;2

Liu, C., Williams, E. R., Zipser, E. J., & Burns, G. (2010). Diurnal variations of global thunderstorms and electrified shower clouds and their contribution to the global electrical circuit. *Journal of the Atmospheric Sciences*, *67*(2), 309–323. https://doi.org/10.1175/2009JAS3248.1

Lucas, G. M., Baumgaertner, A. J. G., & Thayer, J. P. (2015). A global electric circuit model within a community climate model. *Journal of Geophysical Research: Atmospheres*, *120*, 12,054–12,066. https://doi.org/10.1002/2015JD023562

Mach, D. M., Blakeslee, R. J., & Bateman, M. G. (2011). Global electric circuit implications of combined aircraft storm electric current measurements and satellite-based diurnal lightning statistics. *Journal of Geophysical Research*, *116*, D05201. https://doi.org/10.1029/2010JD014462

Mareev, E. A. (2010). Global electric circuit research: Achievements and prospects. *Physics-Uspekhi*, *53*(5), 504–511. https://doi.org/10.3367/UFNe.0180.201005h.0527

Mareev, E. A., & Dementyeva, S. O. (2017). The role of turbulence in thunderstorm, snowstorm, and dust storm electrification. *Journal of Geophysical Research: Atmospheres*, *122*, 6976–6988. https://doi.org/10.1002/2016JD026150

Mareev, E. A., & Volodin, E. M. (2014). Variation of the global electric circuit and ionospheric potential in a general circulation model. *Geophysical Research Letters*, *41*, 9009–9016. https://doi.org/10.1002/2014GL062352

Markson, R. (1986). Tropical convection, ionospheric potentials and global circuit variation. *Nature*, *320*(6063), 588–594. https://doi.org/10.1038/320588a0

Markson, R. (2007). The global circuit intensity: Its measurement and variation over the last 50 years. *Bulletin of the American Meteorological Society*, *88*(2), 223–241. https://doi.org/10.1175/BAMS-88-2-223

Markson, R., Ruhnke, L. H., & Williams, E. R. (1999). Global scale comparison of simultaneous ionospheric potential measurements. *Atmospheric Research*, *51*(3–4), 315–321. https://doi.org/10.1016/S0169-8095(99)00016-2

Mauchly, S. J. (1921). Note on the diurnal variation of the atmospheric-electric potential-gradient. *Physical Review*, *18*(2), 161–162. In Proceedings of the American Physical Society. https://doi.org/10.1103/PhysRev.18.85

Mauchly, S. J. (1923). On the diurnal variation of the potential gradient of atmospheric electricity. *Terrestrial Magnetism and Atmospheric Electricity*, *28*(3), 61–81. https://doi.org/10.1029/TE028i003p00061

Mezuman, K., Price, C., & Galanti, E. (2014). On the spatial and temporal distribution of global thunderstorm cells. *Environmental Research Letters*, *9*(12), 124,023. https://doi.org/10.1088/1748-9326/9/12/124023

Mühleisen, R. (1977). The global circuit and its parameters. In H. Dolezalek, & R. Reiter (Eds.), *Electrical processes in atmospheres* (pp. 467–476). Darmstadt: Steinkopff. https://doi.org/10.1007/978-3-642-85294-7_73

Norville, K., Baker, M., & Latham, J. (1991). A numerical study of thunderstorm electrification: Model development and case study. *Journal of Geophysical Research*, *96*(D4), 7463–7481. https://doi.org/10.1029/90JD02577

Peterson, M., Deierling, W., Liu, C., Mach, D., & Kalb, C. (2017). A TRMM/GPM retrieval of the total mean generator current for the global electric circuit. *Journal of Geophysical Research: Atmospheres*, *122*, 10,025–10,049. https://doi.org/10.1002/2016JD026336

Peterson, M., Liu, C., Mach, D., Deierling, W., & Kalb, C. (2015). A method of estimating electric fields above electrified clouds from passive microwave observations. *Journal of Atmospheric and Oceanic Technology*, *32*(8), 1429–1446. https://doi.org/10.1175/JTECH-D-14-00119.1

Powers, J. G., Klemp, J. B., Skamarock, W. C., Davis, C. A., Dudhia, J., Gill, D. O., et al. (2017). The Weather Research and Forecasting model: Overview, system efforts, and future directions. *Bulletin of the American Meteorological Society*, *98*(8), 1717–1737. https://doi.org/10.1175/BAMS-D-15-00308.1

Pruppacher, H. R., & Klett, J. D. (2010). *Microphysics of clouds and precipitation* (2nd ed.). Dordrecht: Springer.

Romps, D. M., Charn, A. B., Holzworth, R. H., Lawrence, W. E., Molinari, J., & Vollaro, D. (2018). CAPE times P explains lightning over land but not the land-ocean contrast. *Geophysical Research Letters*, *45*, 12,623–12,630. https://doi.org/10.1029/2018GL080267

Romps, D. M., Seeley, J. T., Vollaro, D., & Molinari, J. (2014). Projected increase in lightning strikes in the United States due to global warming. *Science*, *346*(6211), 851–854. https://doi.org/10.1126/science.1259100

Rust, W. D., & Moore, C. B. (1974). Electrical conditions near the bases of thunderclouds over New Mexico. *Quarterly Journal of the Royal Meteorological Society*, *100*(425), 450–468. https://doi.org/10.1002/qj.49710042516

Rycroft, M. J., Harrison, R. G., Nicoll, K. A., & Mareev, E. A. (2008). An overview of Earth's global electric circuit and atmospheric conductivity. *Space Science Reviews*, *137*(1–4), 83–105. https://doi.org/10.1007/s11214-008-9368-6

Rycroft, M. J., Israelsson, S., & Price, C. (2000). The global atmospheric electric circuit, solar activity and climate change. *Journal of Atmospheric and Solar-Terrestrial Physics*, *62*(17–18), 1563–1576. https://doi.org/10.1016/S1364-6826(00)00112-7

Skamarock, W. C., Klemp, J. B., Dudhia, J., Gill, D. O., Barker, D., Duda, M. G., et al. (2008). A description of the Advanced Research WRF Version 3: NCAR Technical Note NCAR/TN-475+STR. https://doi.org/10.5065/D68S4MVH

Slyunyaev, N. N., Ilin, N. V., & Mareev, E. A. (2019). Modeling contributions of continents and oceans to the diurnal variation of the global electric circuit. *Geophysical Research Letters*, *46*, 5516–5525. https://doi.org/10.1029/2019GL083166

Slyunyaev, N. N., Mareev, E. A., Kalinin, A. V., & Zhidkov, A. A. (2014). Influence of large-scale conductivity inhomogeneities in the atmosphere on the global electric circuit. *Journal of the Atmospheric Sciences*, *71*(11), 4382–4396. https://doi.org/10.1175/JAS-D-14-0001.1

Slyunyaev, N. N., Mareev, E. A., & Zhidkov, A. A. (2015). On the variation of the ionospheric potential due to large-scale radioactivity enhancement and solar activity. *Journal of Geophysical Research: Space Physics*, *120*, 7060–7082. https://doi.org/10.1002/2015JA021039

Slyunyaev, N. N., & Zhidkov, A. A. (2016). On parameterization of the global electric circuit generators. *Radiophysics and Quantum Electronics*, *59*(3), 199–216. https://doi.org/10.1007/s11141-016-9689-3

Standler, R. B., & Winn, W. P. (1979). Effects of coronae on electric fields beneath thunderstorms. *Quarterly Journal of the Royal Meteorological Society*, *105*(443), 285–302. https://doi.org/10.1002/qj.49710544319

Tinsley, B. A. (2008). The global atmospheric electric circuit and its effects on cloud microphysics. *Reports on Progress in Physics*, *71*(6), 66,801. https://doi.org/10.1088/0034-4885/71/6/066801

Tinsley, B. A., & Zhou, L. (2006). Initial results of a global circuit model with variable stratospheric and tropospheric aerosols. *Journal of Geophysical Research*, *111*, D16205. https://doi.org/10.1029/2005JD006988

Torreson, O. W., Parkinson, W. C., Gish, O. H., & Wait, G. R. (1946). *Ocean atmospheric-electric results (Scientific results of Cruise VII of the Carnegie during 1928–1929 under command of Captain J. P. Ault, Oceanography—III)*. Washington, DC: Carnegie Institution of Washington. Retrieved from https://archive.org/details/oceanatmospheric00carn (Carnegie Institution of Washington Publication 568).

Whipple, F. J. W. (1929). On the association of the diurnal variation of electric potential gradient in fine weather with the distribution of thunderstorms over the globe. *Quarterly Journal of the Royal Meteorological Society*, *55*(229), 1–18. https://doi.org/10.1002/qj.49705522902

Whipple, F. J. W., & Scrase, F. J. (1936). *Point discharge in the electric field of the Earth: An analysis of continuous records obtained at Kew Observatory*. London: H. M. Stationery Off. Geophys. Mem. No. 68.

Williams, E. R. (2009). The global electrical circuit: A review. *Atmospheric Research*, *91*(2–4), 140–152. https://doi.org/10.1016/j.atmosres.2008.05.018

Williams, E., & Mareev, E. (2014). Recent progress on the global electrical circuit. *Atmospheric Research*, *135–136*, 208–227. https://doi.org/10.1016/j.atmosres.2013.05.015

Williams, E., & Stanfill, S. (2002). The physical origin of the land–ocean contrast in lightning activity. *Comptes Rendus Physique*, *3*(10), 1277–1292. https://doi.org/10.1016/S1631-0705(02)01407-X